Experimental Study of Radiative Sky Cooling Effect for Visibly Transparent, High-Emissivity Glass Windows

by

Antonio Jose Trujillo II

A Thesis Presented in Partial Fulfillment
of the Requirements for the Degree
Master of Science

Approved November 2022 by the
Graduate Supervisory Committee:

Liping Wang, Co-Chair
Patrick Phelan, Co-Chair
Konrad Rykaczewski

ARIZONA STATE UNIVERSITY

December 2022

ABSTRACT

Windows are one of the most significant locations of heat transfer through a building envelope. In warm climates, it is important that heat gain through windows is minimized. Heat transfer through a window glazing occurs by all major forms of heat transfer (convection, conduction, and radiation). Convection and conduction effects can be limited by manipulating the thermal properties of a window's construction. However, radiation heat transfer into a building will always occur if a window glazing is visibly transparent. In an effort to reduce heat gain through the building envelope, a window glazing can be designed with spectrally selective properties. These spectrally selective glazings would possess high reflectivity in the near-infrared (NIR) regime (to prevent solar heat gain) and high emissivity in the atmospheric window, 8-13μm (to take advantage of the radiative sky cooling effect).

The objective of this thesis is to provide a comprehensive study of the thermal performance of a visibly transparent, high-emissivity glass window. This research proposes a window constructed by coating soda lime glass in a dual layer consisting of Indium Tin Oxide (ITO) and Polyvinyl Fluoride (PVF) film. The optical properties of this experimental glazing were measured and demonstrated high reflectivity in the NIR regime and high emissivity in the atmospheric window. Outdoor field tests were performed to experimentally evaluate the glazing's thermal performance. The thermal performance was assessed by utilizing an experimental setup intended to mimic a building with a skylight. The proposed glazing experimentally demonstrated reduced indoor air temperatures compared to bare glass, ITO coated glass, and PVF coated glass.

A theoretical heat transfer model was developed to validate the experimental results. The results of the theoretical and experimental models showed good agreement. On average, the theoretical model demonstrated 0.44% percent error during the daytime and 0.52% percent error during the nighttime when compared to the experimentally measured temperature values.

DEDICATION

I would like to dedicate this thesis to my family and friends. Without their continued support, this research would not have been possible. First and foremost, I would like to thank my parents, Melissa and Antonio Trujillo Sr., for their seemingly endless love. I will never truly understand the sacrifices that you have made for me, but I appreciate every one of them. Next, I would like to thank my brothers, Dennis, Brandon, and Alexander, for motivating me to strive for more. Finally, I would like to thank my friends, Emily Jones, Zachary Marlin, and Alvar Rayne, for always believing in me and cheering me on.

I would also like to dedicate this thesis to Monster Energy®, all-nighters, and late-night Circle K runs. My academic journey would be incomplete without them.

ACKNOWLEDGMENTS

I would like to thank my thesis co-chairs, Dr. Liping Wang and Dr. Patrick Phelan, for presenting me with this research opportunity and for their guidance in my academic career. I would also like to thank my final committee member, Dr. Konrad Rykaczewski, for his patience and support leading up to my thesis defense.

TABLE OF CONTENTS

Page

LIST OF FIGURES

Figure Page

Figure Page

Figure Page

LIST OF VARIABLES

q_i — Net radiative heat flux leaving surface i within the model envelope

$q_{rad,net}$ — Net radiative heat flux leaving the skyward facing surface of glazing

h_i — Internal convective heat transfer coefficient

h_o — External convective heat transfer coefficient

T_i — Temperature of surface i within the model envelope

T_∞ — Temperature of air within model enclosure

T_a — Temperature of outdoor ambient air

δ_{ij} — Kronecker delta

F_{ij} — View factor for radiation leaving surface i striking surface j

$E_{b\lambda j}$ — Spectral blackbody emissive power of surface j

$\varepsilon_{\lambda j}$ — Spectral emissivity of surface j

$q_{\lambda j}$ — Spectral radiative heat flux leaving surface j

$H_{o\lambda i}$ — Spectral external irradiation incident on surface i

q_{emit} — Total heat flux radiated by the glazing

q_{atm} — Total heat flux radiated by the atmosphere that is absorbed by the glazing

q_{sun} — Total solar heat flux absorbed by the glazing

I_{BB} — Spectral radiance of a black body

h — Planck's constant

c — Speed of light in a vacuum

k_B — Boltzmann constant

$G_{AM1.5}$ — Air mass 1.5 global tilt spectrum

x — Scaling factor for air mass 1.5 global tilt spectrum

I_{atm} — Spectral, directional, atmospheric irradiance

Nu — Nusselt Number

H — Height of model

L — Length of glazing

k_{air} — Thermal conductivity of air

Ra — Rayleigh number

Gr — Grashof number

Re — Reynolds number

Pr — Prandtl number

V_{wind} — Wind speed

G_{sun} — Total solar flux

τ_{λ} — Spectral transmissivity

ρ_{λ} — Spectral reflectivity

$U_{T_{\infty}}$ — Total uncertainty of inner air temperature

$B_{T_{\infty}}$ — Bias uncertainty of inner air temperature

$P_{T_{\infty}}$ — Precision uncertainty of inner air temperature

B_{T_a} — Bias uncertainty of outdoor air temperature measurement

B_V — Bias uncertainty of wind speed measurement

B_G — Bias uncertainty of total solar flux measurement

CHAPTER 1

INTRODUCTION

1.1 Background

Windows are a vital part of standard building construction because they provide occupants with an unobstructed view of their surroundings as well as daytime lighting. Unfortunately, windows are responsible for up to 60% of a building's total energy loss [1]; this energy loss increases cooling loads in warm climates. Unwanted energy gain through any fenestration is caused by a combination of heat and mass transfer. Mass transfer can be outright eliminated by preventing air leakage into the building envelope. However, heat transfer through windows cannot be eliminated if the glazing is visibly transparent, or a temperature differential exists between the outdoor and indoor environments. Visibly transparent glazing will always allow heat gain from solar irradiation in the visible spectrum, and a temperature differential between the outdoor and indoor air environments will cause heat flow via convection and conduction. The effect of convective and conductive heat transfer can be reduced by decreasing a window's thermal transmittance (U-value). U-values are decreased by manipulating the thermal properties of the window construction. This is most commonly accomplished through the use of multi-layer glazing [1]. The effect of solar heat gain (and other forms of radiative heat transfer) can be minimized by manipulating the optical properties of the glazing.

In order to minimize radiative heat gains while maintaining visibility, a window glazing must exhibit specific spectral properties that vary with wavelengths; this is known as spectral selectivity. In general, thermal radiation can be divided into three

major regimes: visible, near-infrared (NIR), and mid-infrared (MIR). Solar irradiation, the main source of radiative heat gain, spans wavelengths of light ranging from 0.28 μm to 2.5 μm. The solar spectrum has a maximum total irradiance of about 1000 Wm^{-2}, with about 4% being in the ultraviolet (UV) spectrum, 43% being in the visible spectrum, and 53% being in the NIR spectrum [2]. Fig 1.1 presents the spectral irradiance distribution of the Air Mass (AM) 1.5 Global Tilt Spectrum. The AM 1.5 Global Tilt Spectrum is commonly used to model the solar spectrum in theoretical applications.

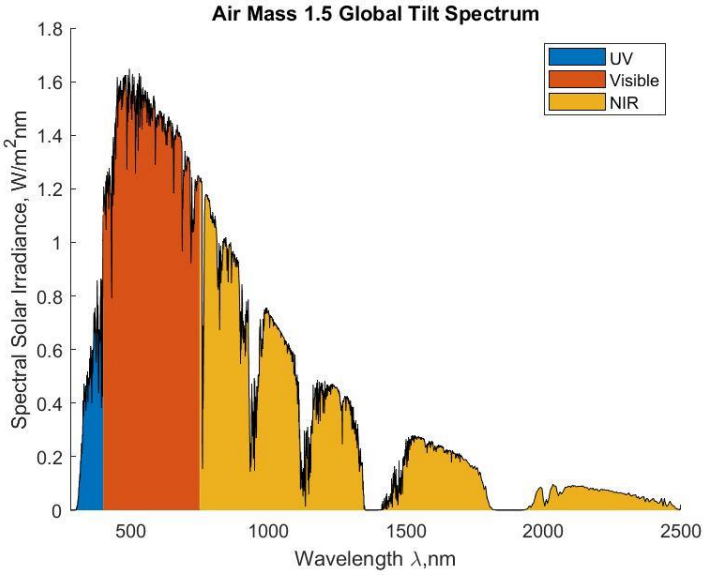

Figure 1.1: Spectral solar irradiance of the Air Mass 1.5 Global Tile Reference Spectrum as a function of wavelength [3].

For a window to provide an unobstructed view of the surroundings, the glazing must have a high transmissivity value (τ) in the visible spectrum. Ideally, the transmissivity value would be unity for wavelengths of light between 0.4 and 0.75μm. Undesirable solar heat gain from the UV and NIR spectrums is minimized by maximizing the glazing reflectivity (ρ) in those regimes. Ideally, the reflectivity of the glazing would be unity for

both the UV and NIR spectrums. However, it is far more crucial that NIR reflectivity is high due to the greater quantity of solar irradiation in this regime. In addition to solar irradiation, unwanted radiative heat gain through windows is caused by atmospheric irradiance as well as thermal emission from other objects in the local environment. These sources of irradiation are localized in the MIR regime. Fig 2.2 presents the spectral distribution of atmospheric irradiance based on the model developed by Mandal et. al. as well as the spectral irradiance emitted from a blackbody at 20℃ as governed by Planck's law.

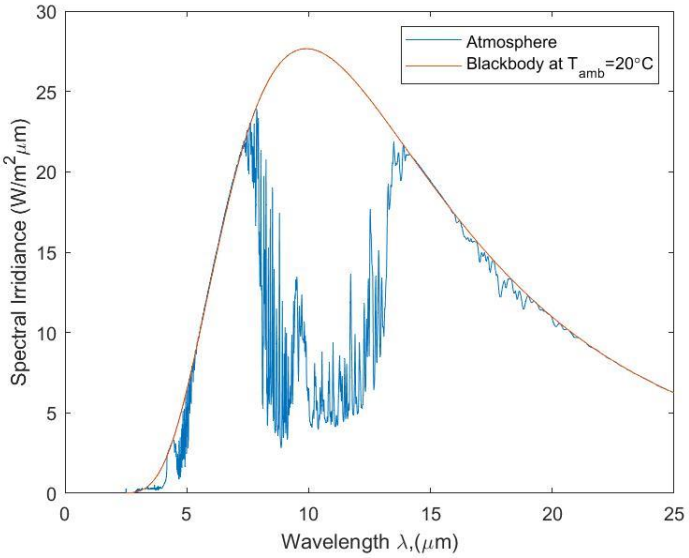

Figure 1.2: Spectral atmospheric irradiance for an ambient temperature of 20℃ compared to the irradiance from a blackbody at equivalent temperature [3].

Like solar radiation in the NIR regime, unwanted heat gain from atmospheric irradiance is prevented by glazing that maximizes reflectivity in the MIR regime. Although thermal emission from other objects in the local environment will contribute to heat gain, thermal emission from the glazing itself provides an opportunity to reject heat in the MIR regime.

The phenomenon of rejecting heat via thermal emission is known as radiative cooling. The main benefit of radiative cooling, as opposed to other means such as HVAC, is that it is passive. When thermal emission is directed at the sky, a phenomenon known as radiative sky cooling occurs. Radiative sky cooling takes advantage of the large temperature differential between deep space ($T_{space} \approx 2.7K$) and the terrestrial environment. Radiative sky cooling is made possible by the high transmissivity of Earth's atmosphere in the 8-13μm regime (known as the atmospheric window) [4]. Radiative sky cooling has only recently demonstrated the capability to produce sub-ambient daytime cooling [5]. The major drawbacks to materials that possess this capability is that they tend to be non-transparent and are often difficult to manufacture on a large scale.

1.2 Literature Review

Neither the use of spectrally selective windows nor the use of radiative cooling is novel. In fact, the use of radiative sky cooling can be seen in Iranian architecture dating back to 900 A.D. for the production of ice [6]. In modern times, research focus leading to the development of "cool" windows can be subdivided into two main areas: prevention of solar heat gain and increasing radiative sky cooling effect. Furthermore, research into passive radiative cooling materials can be subdivided into visibly opaque and visibly transparent materials.

When preventing solar heat gain, it is important for window design to take visibility into consideration. However, it is common for glazing technology to employ techniques that reduce visible transmission (especially in warm climates). In the simplest cases, this involves the use of tinted and reflective glazing. Tinted glazing has high

absorbance leading to reduced solar transmittance; tinted glazing has been shown to reduce the thermal load of a room by up to 22.4% compared to conventional clear glass [7]. Reflective glazing opts to increase the reflectivity of the glazing at the expense of its transmissivity. When compared to tinted glazing, reflective glazing has been shown to have a greater impact on reducing solar transmission, up to 50% [8]. However, reflective glazing also presents issues due to the Sun mirror effect which may cause safety concerns [7]. The constant reduced visible transmissivity of reflective and tinted glazing has been improved upon using chromogenic technology. Chromogenic technology allows for adjustable transmittance properties. During warm conditions, they will toggle to a colored state characterized by low solar transmissivity, and during cold conditions they will toggle to a transparent state characterized by high solar transmissivity [1]. The most developed type of chromogenic window is electrochromic which responds to an electrical voltage/charge; electrochromic windows have been shown to demonstrate a solar transmission modulation of up to 0.68 [1,9]. Instead of reducing transmissivity, solar heat gains can be reduced by increasing reflectivity in the infrared regime. This is commonly achieved by employing Low-emittance (Low-e) coatings. Low-e coatings are essentially metals or metal oxide coatings that have relatively high visible transmissivity and high infrared reflectivity; low-e coatings have been shown to reduce heat gain through windows by 48% [8]. Low-e windows are quite common in the United States (30% market share of installed fenestration products), but they suffer from relatively high production costs [7].

Up until recently, the bulk of research concerning radiative sky cooling has been about visibly opaque materials. Prior to 2014, passive radiative cooling had not achieved sub-ambient cooling during the daytime. This changed when Raman et. al. developed a photonic radiative cooler that demonstrated cooling 4.9℃ below ambient temperature. This cooler had a solar reflectivity of 97% with high emissivity in the atmospheric window [5]. Unfortunately, nanoscale photonic structures are not practical to manufacture due to cost and complexity. As a consequence, research interest has shifted to radiative coolers produced from cheaper, easier to manufacture materials. In 2017, Kou et. al developed a radiative cooler based on a three-layer design comprised of polydimethylsiloxane (PDMS), silica, and silver. This cooler experimentally achieved a stagnation temperature of 8.2℃ below ambient under direct sunlight [10]. Later, Meng et. al. proposed a radiative cooler that utilized a dual layer design comprised of PVF and silver. This cooler experimentally demonstrated a stagnation temperature 2℃ below ambient under solar irradiation of 950 Wm^{-2} [11].

Interest in visibly transparent, passive radiative cooling materials was primarily motivated by the need to keep solar cells cool. Solar cells need to be able to absorb photons that meet the bandgap energy while simultaneously staying cool. Solar cells must stay cool because their performance is dramatically affected by excess heat. A 1℃ increase in operating temperature decreases the efficiency 0.4%-0.5% for crystalline silicon solar cells [12]. To keep solar cells cool, Lee et. al. proposed the use of a pyramid-structured PDMS layer. Calculations showed the potential to decrease the temperature of organic, perovskite, and micro-crystalline (μc)-Si flexible solar cells by 11℃, 12℃ and

16℃, respectively [13]. Recently attention has shifted towards the application of visibly transparent, radiative cooling materials in buildings, namely window glazing. Yi et. al. proposed a transparent radiative cooling film made of polyethylene terephthalate (PET) and silica microspheres. In an experimental study, the indoor air temperature of two glass roof models was measured, and a max temperature difference of 21.6℃ was recorded between the model fitted with and without the metamaterial on the glass [14]. Recently, Zhang et. al. utilized a multilayer design consisting of PDMS, ITO, and silicon dioxide applied to a glass substrate to develop a radiative cooling window. With a similar experimental setup as Yi et. al., this radiative cooling window demonstrated a maximum indoor air temperature reduction of 18.1℃ compared to conventional glass [15].

1.3 Objectives

The primary objective of this research is to provide a comprehensive study of the radiative sky cooling effect for a visibly transparent, high-emissivity glass window. It is hypothesized that the use of a multi-layer design consisting of commercially sourced, Polyvinyl Fluoride (PVF) film and Indium Tin Oxide (ITO) coating applied to a Soda Lime glass substrate will demonstrate superior day and nighttime cooling effect compared to conventional glass windows. It is predicted that the PVF film will provide improved radiative sky cooling effect due to its high emissivity in the atmospheric window, and the ITO coating will decrease solar heat gain due to its high reflectivity in the infrared regime.

In addition to this introductory chapter, this thesis will contain three more chapters. Chapter 2 details a heat transfer model used to validate temperature

distributions and cooling performance associated with the experimental test setup described in Chapter 3. Chapter 3 discusses results found from field testing performed with the experimental setup. Additionally, Chapter 3 presents the measured spectral properties of the proposed window glazing. Finally, Chapter 4 discusses conclusions and opportunities for future work.

CHAPTER 2

THEORETICAL MODELLING

2.1 Heat Transfer Model of Window System

A heat transfer model was developed to predict the temperature distribution within the experimental setup. The experimental setup and consequently the theoretical model is meant to mimic a building with a skylight. The nominal geometry used in the theoretical model is shown in Fig. 2.1. For a given solar flux, wind speed, and outdoor ambient temperature, the heat transfer model calculates the temperature values of the inner model surfaces as well as the enclosed air.

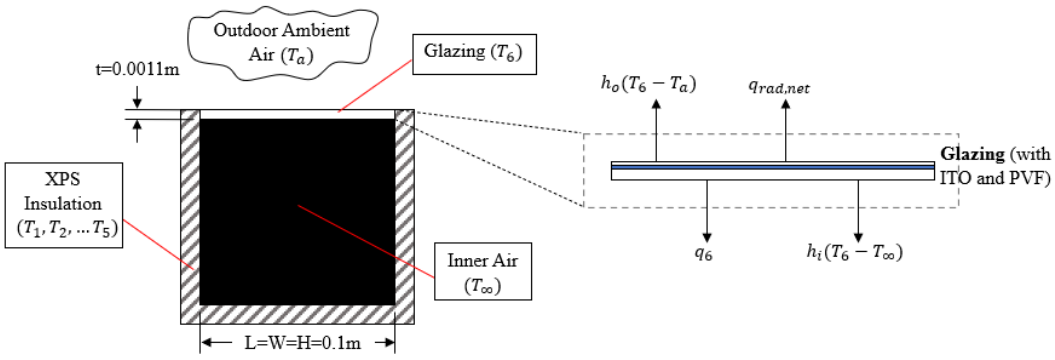

Figure 2.1: 2D schematic of experimental setup with heat flows displayed for glazing surface.

Since the heat transfer model is used to evaluate seven unknown temperature values, seven independent equations are necessary to constrain the system. These seven equations appear as such:

$$q_1 + h_i(T_1 - T_\infty) = 0 \quad (\mathbf{1})$$

$$q_2 + h_i(T_2 - T_\infty) = 0 \quad (\mathbf{2})$$

$$q_3 + h_i(T_3 - T_\infty) = 0 \quad (\mathbf{3})$$

$$q_4 + h_i(T_4 - T_\infty) = 0 \quad (\mathbf{4})$$

$$q_5 + h_i(T_5 - T_\infty) = 0 \quad (\mathbf{5})$$

$$q_6 + q_{rad,net} + h_o(T_6 - T_a) + h_i(T_6 - T_\infty) = 0 \quad (\mathbf{6})$$

$$h_i \sum_{i=6}^{6} (T_i - T_\infty) = 0 \quad (\mathbf{7})$$

q_i for $i = 1,2, \ldots 6$, is the net radiative heat flux leaving surface i within the model envelope. $q_{rad,net}$ is the net radiative heat flux leaving the skyward facing surface of the glazing. h_i and h_o are the internal and external convective heat transfer coefficients, respectively. T_i for $i = 1,2, \ldots 6$ is the temperature of surface i, within the model envelope. T_∞ is the temperature of the air confined within the model, and T_a is the outdoor ambient air temperature.

Equations (1)-(6) represent the steady-state energy balance on the inner surfaces of the experimental setup. The floor surface is represented by equation (1). The wall surfaces are represented by equations (2)-(5). The glazing/roof surface is represented by equation (6). Heat flows given in equation (6) are presented as a schematic in Fig 2.1. Finally, equation (7) represents the steady-state energy balance on the air confined within experimental setup.

The net radiative heat flex leaving surfaces within the enclosure is calculated by solving the system of equations represented by equation (8) for $q_{\lambda j}$ and integrating over the entire spectrum [16].

$$\sum_{j=1}^{6}\left[\delta_{ij}-F_{ij}\right]E_{b\lambda j}=\sum_{j=1}^{6}\left[\frac{\delta_{ij}}{\varepsilon_{\lambda j}}-\left(\frac{1}{\varepsilon_{\lambda j}}-1\right)F_{ij}\right]q_{\lambda j}+H_{o\lambda i}, \quad (\mathbf{8})$$

δ_{ij} is the Kronecker delta. F_{ij} is the view factor for radiation leaving surface i striking surface j. $E_{b\lambda j}$ is the spectral black body emissive power (as governed by Planck's law) of surface j. $\varepsilon_{\lambda j}$ is the spectral emissivity of surface j. $q_{\lambda j}$ is the net spectral radiative heat flux leaving surface j. $H_{o\lambda i}$ is the external spectral irradiation incident on surface i.

Recall, $q_{rad,net}$ refers to the net radiative heat flux leaving the sky-facing surface of the glazing.

$$q_{rad,net}=q_{emit}-q_{atm}-q_{sun} \quad (\mathbf{9})$$

In equation (9), q_{emit}, q_{atm}, and q_{sun} are the total heat flux radiated by the glazing, total heat flux radiated by the atmosphere that is absorbed by the glazing, and total solar heat flux absorbed by the glazing, respectively. The value of these terms are calculated using equations (10)-(12):

$$q_{emit}=\int_0^{\infty}\int_0^{2\pi}\int_0^{\frac{\pi}{2}}I_{BB}(\lambda,T_6)\varepsilon_{\lambda,\theta}(\lambda,\theta,\phi)\cos(\theta)\sin(\theta)\,d\theta d\phi d\lambda \quad (\mathbf{10})$$

$$q_{sun}=\int_0^{\infty}xG_{AM1.5}(\lambda)\varepsilon_{\lambda}d\lambda \quad (\mathbf{11})$$

$$q_{atm}=\int_0^{\infty}\int_0^{2\pi}\int_0^{\frac{\pi}{2}}I_{atm}(\theta,\lambda,T_a)\varepsilon_{\lambda,\theta}(\lambda,\theta,\phi)\cos(\theta)\sin(\theta)\,d\theta d\phi d\lambda \quad (\mathbf{12})$$

$I_{BB}(\lambda,T_6)$ is the spectral radiance of the glazing surface given by Planck's law.

$$I_{BB}(\lambda,T)=\frac{2hc^2}{\lambda^5\left[e^{\frac{hc}{\lambda k_B T}}-1\right]} \quad (\mathbf{13})$$

In Planck's law, the variables h, c, and k_B are Planck's constant, the speed of light in a vacuum, and the Boltzmann constant, respectively. The spectral, directional emittance of the glazing is given by $\varepsilon_{\lambda,\theta}$. The spectral, directional emittance is used in lieu of the spectral, directional absorptivity in equations (10) and (12) due to their equality under Kirchhoff's law. $G_{AM1.5}$ represents the Air Mass 1.5 Global Tilt Spectrum, and it is used to represent the incident solar radiation [3]. The variable x found in equation (11) is a scaling factor used to preserve the spectral behavior of the global tilt spectrum while scaling for a measured total solar flux. Finally, I_{atm} is the spectral, directional, atmospheric irradiance based on the model developed by Mandal et. al [3].

As evident, the main modes of heat transfer acting on the model are radiation and convection. Only natural convection occurs within the model envelope. The convection coefficient for the air within the envelope, h_i, is calculated using the Nusselt number relation for enclosures developed by Rincón-Casado et. al [17].

$$Nu = \frac{h_i L}{k_{air}} = \begin{cases} 0.083 * Ra_L^{0.339} * \left(\frac{H}{L}\right)^{-0.095} & 10^3 < Ra_L < 10^7 \\ 0.4378 * Ra_L^{0.258} * \left(\frac{H}{L}\right)^{-0.488} & 10^7 < Ra_L < 10^{11} \end{cases} \quad (\mathbf{14})$$

In equation (14), H is the height of the enclosure, and L is the length of the enclosure. Outside the building envelope, a combination of natural and forced convection effects are present. The convection coefficient for the air outside the building envelope, h_o, can also be calculated using Nusselt number relations [18]. When forced convection dominates, ($\frac{Gr}{Re^2} < 0.1$), h_o is calculated using equation (15). When natural convection dominates ($\frac{Gr}{Re^2} > 10$), h_o is calculated using equation (16). When neither natural nor forced

convection dominates $0.1 < \frac{Gr}{Re^2} < 10$, h_o is calculated using equation (17); the terms Nu_F (forced convection Nusselt number) and Nu_N (natural convection Nusselt number) are calculated using equation (15) and (16), respectively.

$$Nu_F = \frac{h_o L}{k_{air}} = \begin{cases} 0.664 Re_L^{0.5} Pr^{\frac{1}{3}} & Re_L < 5 * 10^5 \\ 0.037 Re_L^{0.8} Pr^{\frac{1}{3}} & 5 * 10^5 < Re_L < 10^7 \end{cases} \quad (\mathbf{15})$$

$$Nu_N = \frac{h_o L}{k_{air}} = \begin{cases} 0.54 Ra_L^{\frac{1}{4}} & T_6 > T_a, 10^4 < Ra_L < 10^7 \\ 0.15 Ra_L^{\frac{1}{3}} & T_6 > T_a, 10^7 < Ra_L < 10^{11} \\ 0.27 Ra_L^{\frac{1}{4}} & T_6 < T_a, 10^5 < Ra_L < 10^{11} \end{cases} \quad (\mathbf{16})$$

$$Nu_{comb} = \frac{h_o L}{k_{air}} = (Nu_F^{3.5} + Nu_N^{3.5})^{\frac{1}{3.5}} \quad (\mathbf{17})$$

2.2 Predicted Thermal Performance

The thermal performance of various glazings was calculated using the system of governing equations presented in the previous section. The window glazings being assessed are bare soda-lime glass, soda-lime glass covered in PVF film, soda-lime glass coated in ITO, and soda-lime glass coated in ITO and PVF film. When evaluating the thermal performance of the each of these glazings, the optical properties used in the subsequent calculations were measured using UV-visible spectroscopy and Fourier transform infrared spectroscopy (FTIR); further details of spectroscopy measurements are discussed in chapter 3. However, the wall and floor surfaces of the inner enclosure were modelled as blackbodies for the theoretical calculations in this chapter. This choice was made to gain better insight on the cooling performance of the experimental glazings. Since the experimental model is intended to mimic a building, the primary indicator of

thermal performance is the internal air temperature. Given that the goal of the windows is prevent excess heat gain and maximize cooling, superior glazing performance is characterized by low internal air temperature values.

As discussed previously, the only inputs to the theoretical model are the solar flux, wind speed, and outdoor ambient temperature. Since wind speed only impacts convective heat transfer, it is most beneficial to assess the effect of varying solar flux and outdoor ambient temperature. The outdoor air temperature is directly related to the global solar radiation [19]. For simplicity, the effect of independently varying the outdoor air temperature for full sun (shown in Fig. 2.2) and no sun (shown in Fig. 2.3) conditions was assessed.

For both day and nighttime conditions, internal air temperature increases with increasing outdoor ambient air temperature, irrespective of glazing type. During the day, inner air temperature values are significantly larger than those at night at equivalent outdoor temperatures because of the solar heating effect. As expected, the glazing with ITO and PVF demonstrated the greatest cooling capability irrespective of ambient air temperature. The proposed glazing had a theoretical internal air temperature roughly 8℃ cooler than conventional glass. Furthermore, the trend between the remaining glazings appeared as expected. Despite its high reflectivity, the ITO coated glazing's lack of cooling capability contributed to it having the largest theoretical inner air temperature. The glazing with PVF only had slightly better cooling performance that conventional glass likely due to the increased emissivity in the atmospheric window.

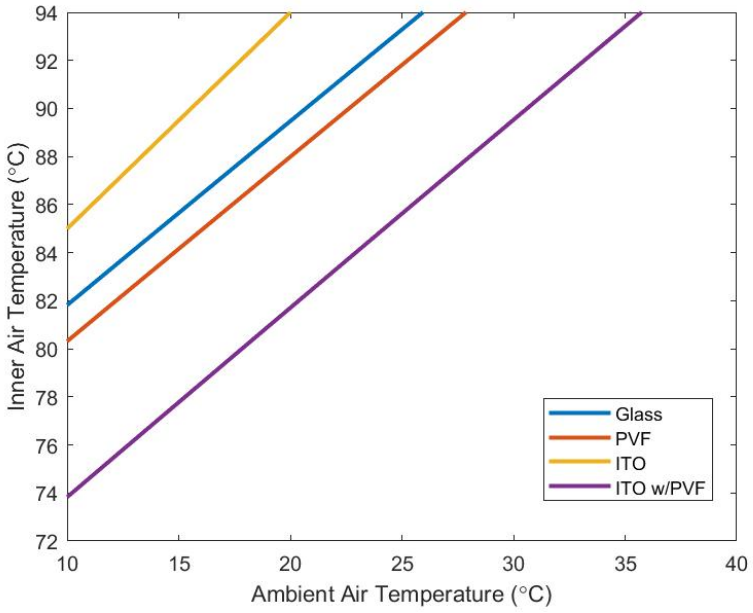

Figure 2.2: Theoretically predicted model air temperature for real glazings as a function of T_a for V_{wind}=0.5m/s and full sun ($G_{sun} = G_{AM1.5}$) conditions.

During no-sun conditions, the proposed glazing with ITO and PVF film demonstrated near identical theoretical cooling performance compared to the glazing with PVF only. Both glazings with PVF demonstrated a small, but insignificant cooling benefit compared to conventional glass. Similar to the daytime conditions, the glazing coated only in ITO demonstrated the worst theoretical cooling performance. However, all glazing models theoretically predicted sub-ambient inner air temperatures.

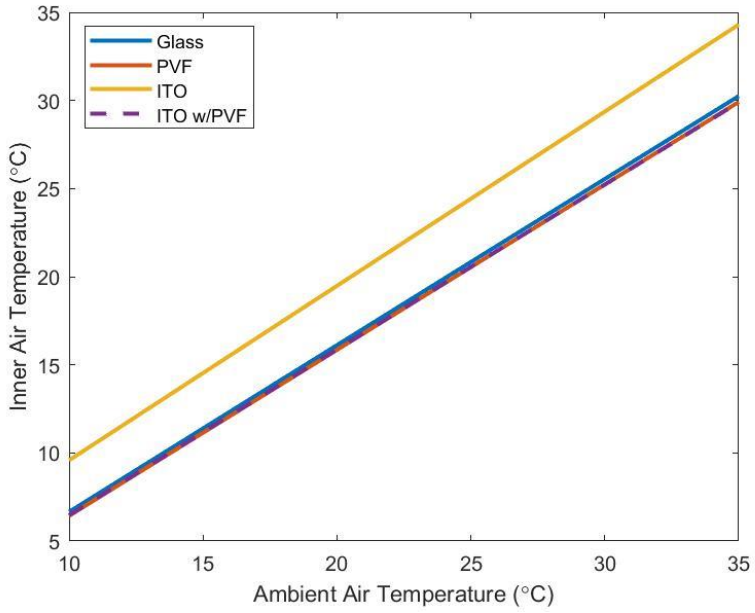

Figure 2.3: Theoretically predicted model air temperature for real glazings as a function of T_a for V_{wind}=0.5m/s and full sun ($G_{sun} = 0$) conditions.

To gain a deeper understanding of the solar heating effect, the total solar spectral properties were calculated theoretically. This involves the use of equation (11). The value of x in equation (11) is taken as 1 to represent full sun conditions. In order to determine the total solar irradiation transmitted and reflected by the glazings, equation (11) is modified by replacing the spectral emissivity with the spectral transmissivity and reflectivity, respectively. From Fig. 2.4, it is evident that the proposed glazing demonstrates the least solar transmittance of all the glazings being investigated. This will inevitably lead to less solar heat gain.

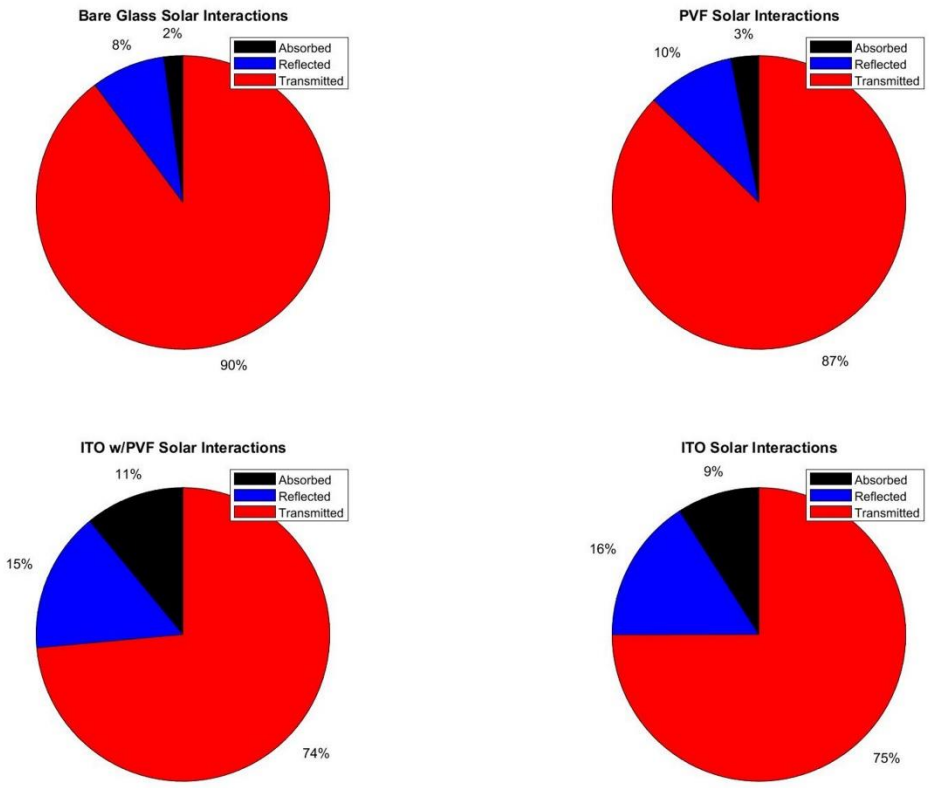

Figure 2.4: Total solar spectral properties for real glazings.

2.3 Ideal Glazing Performance

It is convenient to assess the theoretical performance of the experimental window glazing by comparing it to common idealized cases. The cases of interest are idealized Low-e glazing, idealized radiative cooling glazing without solar heat gain prevention, and an idealized radiative cooling glazing with solar heat gain prevention. For the rest of the theory section, these will be referred to as ideal Low-e, ideal RC, and ideal window glazing, respectively. Ideal low-e glazing utilizes high reflectivity outside the visible spectrum to prevent unwanted solar heat gain but does not produce radiative sky cooling effect. Ideal RC glazing does not prevent solar heat gain (high transmissivity in solar

spectrum) but has high emissivity in the atmospheric window to produce radiative sky cooling effect. The ideal window has high reflectivity in the NIR to prevent unwanted solar heat gain and has high emissivity in the atmospheric window to produce a greater radiative sky cooling effect. For this analysis, the idealized window glazings will have their characteristic spectral properties (presented in Fig. 2.5, Fig. 2.6, and Fig. 2.7) on its sky-facing surface.

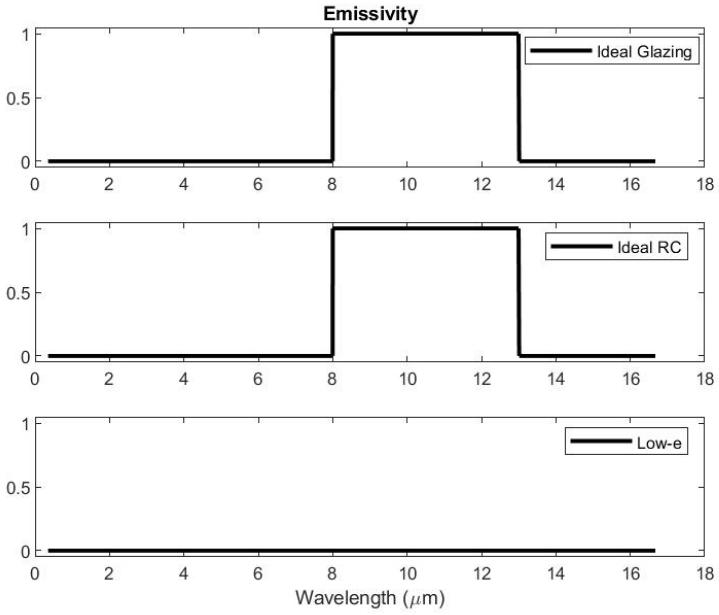

Figure 2.5: Spectral Emissivity of various ideal glazings.

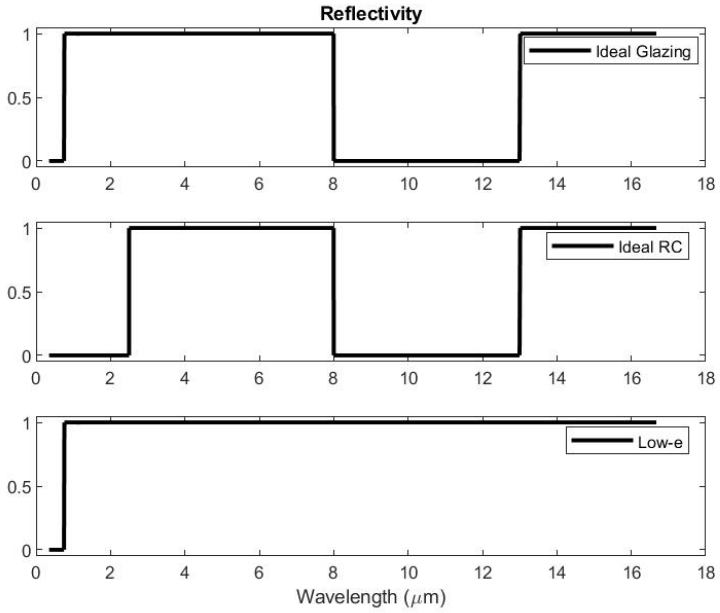

Figure 2.6: Spectral Reflectivity of various ideal glazings.

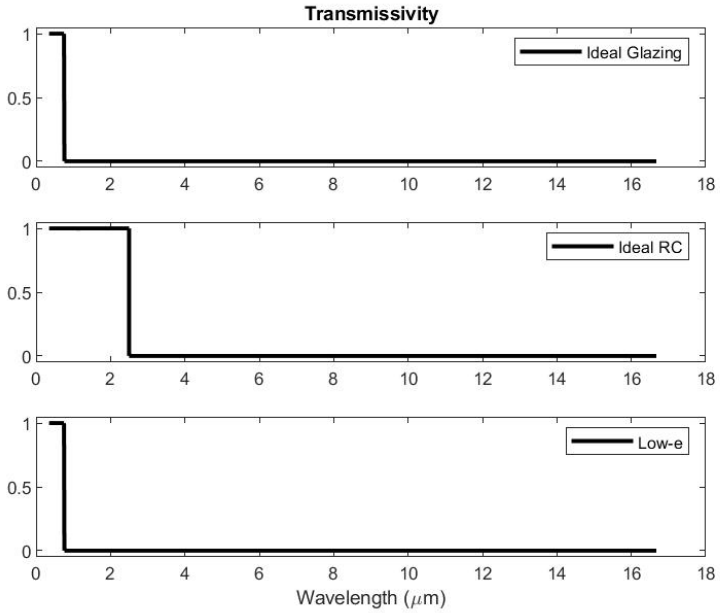

Figure 2.7: Spectral Transmissivity of various ideal glazings.

The idealized windows will be modeled as having the same spectral properties as the soda-lime glass on the inward facing surface. This is meant to emulate a traditional glass

window with an idealized coating or film on the sky-facing surface. Furthermore, this simplification is acceptable as thermal radiation exchange within the building envelope is primarily within the MIR regime, and glass is opaque for these wavelengths.

The predicted performance of the idealized glazings under full sun conditions are shown in Fig. 2.8. Similar to the real glazings, the internal air temperature increased with increasing ambient air temperature irrespective of glazing type. The ideal glazing theoretically performed the best. In fact, the inner air temperature within the ideal glazing model was roughly 19°C cooler than the proposed window glazing consisting of ITO and PVF film. The second-best performance was the idealized Low-E glazing. Despite not having a radiative cooling effect, it was able to reflect all incoming NIR and MIR leading to a good cooling performance. The idealized RC glazing had the worst cooling performance. Since the ideal RC glazing lacks reflectivity in the solar spectrum, all incident solar irradiation is absorbed by the enclosure floor and walls (modelled as blackbody surfaces).

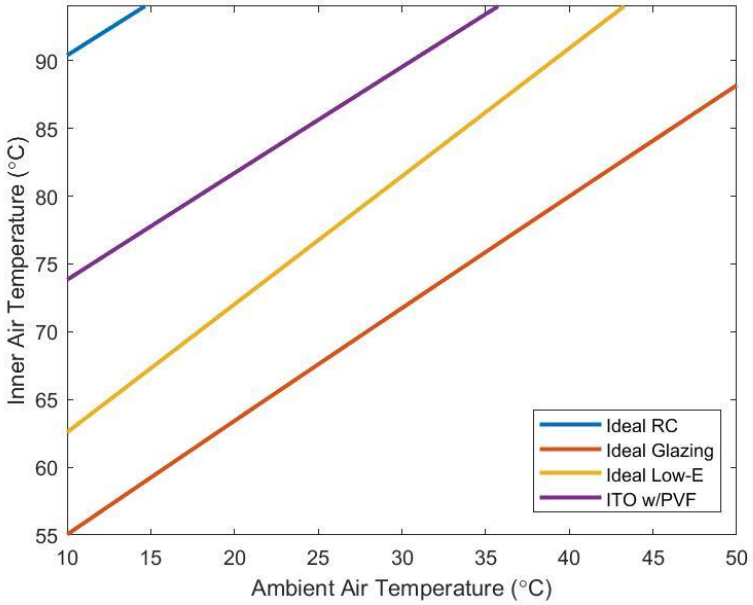

Figure 2.8: Theoretically predicted model air temperature for ideal glazings as a function of T_a for V_{wind}=0.5m/s and full sun ($G_{sun} = G_{AM1.5}$) conditions.

As shown in Fig. 2.9, Ideal RC and Ideal Glazing theoretically predicted the best cooling performance under nighttime conditions. The near identical cooling performance of the Ideal RC glazing and Ideal Glazing is likely due to their identical spectral properties in the atmospheric window. The proposed glazing consisting of ITO and PVF coating had a theoretical inner air temperature that was slightly greater, but comparable to the Ideal glazing. The lack of radiative sky cooling effect likely contributed to the ideal Low-e glazing having worst theoretical cooling performance. All glazings except for the ideal Low-e glazing predict sub-ambient inner air temperatures. The ideal Low-e glazing predicts an inner air temperature that is near identical to the ambient air temperature.

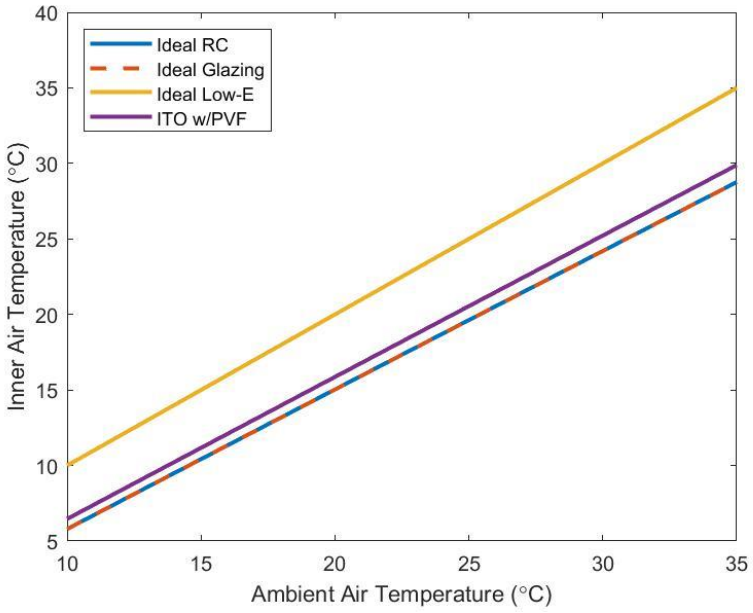

Figure 2.9: Theoretically predicted model air temperature for ideal glazings as a function of T_a for V_{wind}=0.5m/s and no sun ($G_{sun} = 0$) conditions.

Fig. 2.10 displays the theoretical total solar spectral properties for the ideal glazings and the proposed ITO/PVF glazing. It is quite evident that the ITO/PVF glazing could have improved reflectivity and decreased transmissivity to have performance comparable to the ideal glazing in the solar spectrum. As expected, the ideal glazing has identical total solar spectral properties compared to the ideal Low-e glazing. This is because both the ideal Low-e glazing and ideal glazing only transmit visible light in the solar spectrum and reflect the rest.

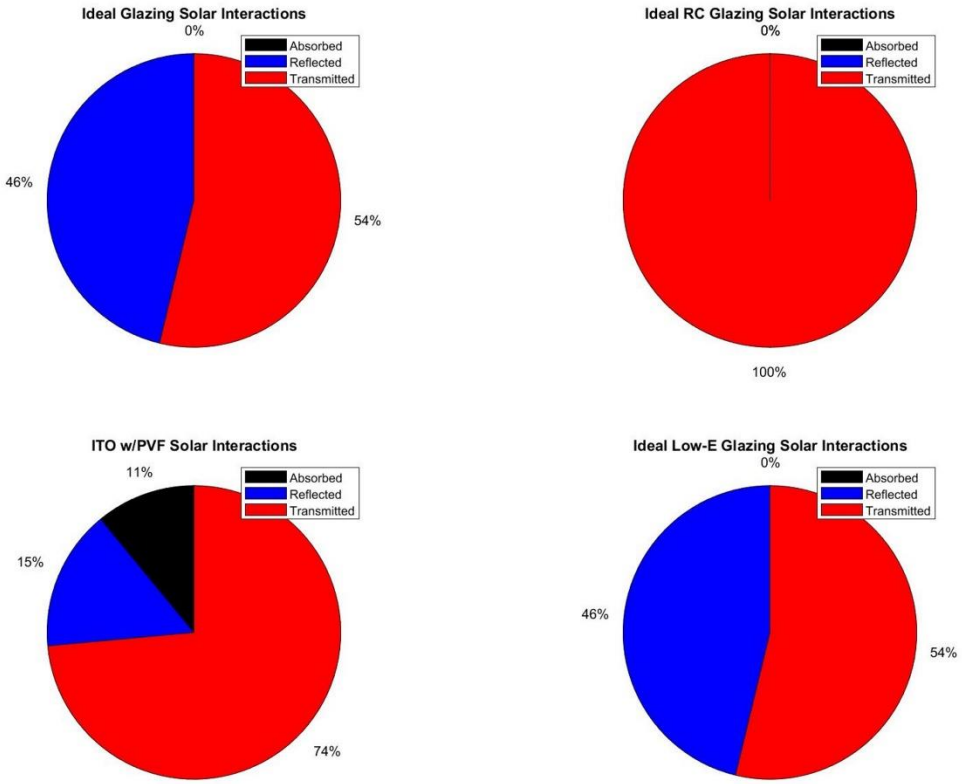

Figure 2.10: Total solar spectral properties for ideal glazings.

CHAPTER 3

EXPERIMENTAL METHODS AND RESULTS

3.1 Experimental Setup

An image of the experimental setup is shown in Fig. 3.1; an anemometer (ennoLogic eA980R) and solar power meter (AMPROBE SOLAR-100) were also used to take experimental measurements but were not included in Fig. 3.1.

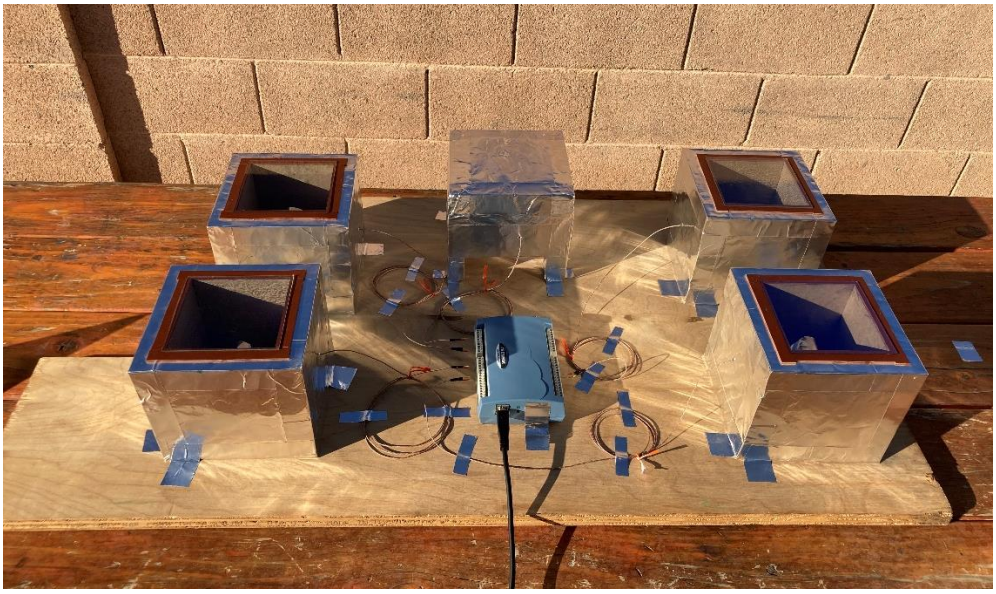

Figure 3.1: Experimental setup for outdoor field test.

K-type thermocouples measured the outdoor ambient air temperature as well as the internal air temperature within the four box models. The K-type thermocouples were connected to a data acquisition (DAQ) system (Omega OM-USB-TEMP) to record the measured temperature values. To prevent erroneous temperature readings due to solar heating, a strip of aluminum foil was used to shield the thermocouple tips. During the daytime hours, the solar power meter was used to measure the total incoming solar flux. During day and nighttime hours, the anemometer was used to measure the wind speed.

The box models were constructed such that the inner envelope was nominally a cube with a side length of 10 cm. The outer facing surfaces of the models were covered in aluminum foil to limit unwanted radiative heat gain. The walls and floor of the models were roughly 2.5 cm thick and constructed from extruded polystyrene (XPS) foam board insulation with an R-value of 5. The inner surfaces of the box models were lined with visibly black construction paper. As seen in Fig 3.1, the pigment of the visibly black construction paper degraded over the length of the experiment. The experimental glazing surfaces served as the roof/skylight of the models. A rubber seal was placed between the glazing surface and walls of the model to prevent undesirable air leakage in (or out) of the model envelope.

Glazing surfaces were constructed using commercially available materials. Bare glass and ITO coated glass substrates were sourced from MSE Supplies LLC. The glass substrates were nominally square with a side length of 10 cm and thickness of 1.1 mm. All glass substrates were made from soda-lime glass. The ITO coating thickness was nominally 185nm, and each sheet of ITO glass had a nominal resistance of 7~10 Ohm/Sq. The ITO coating was applied to only one side of the glass-substrate. Self-adhesive PVF film (DuPont Tedlar®) was sourced from Emedco Inc. The PVF film thickness was nominally 25μm. For the proposed window, the PVF film was applied to the ITO coated side of the glass-substrate. During experimental testing, surfaces coated in ITO and/or PVF faced the sky. Close-up images of the various glazing surfaces are shown in Fig. 3.2.

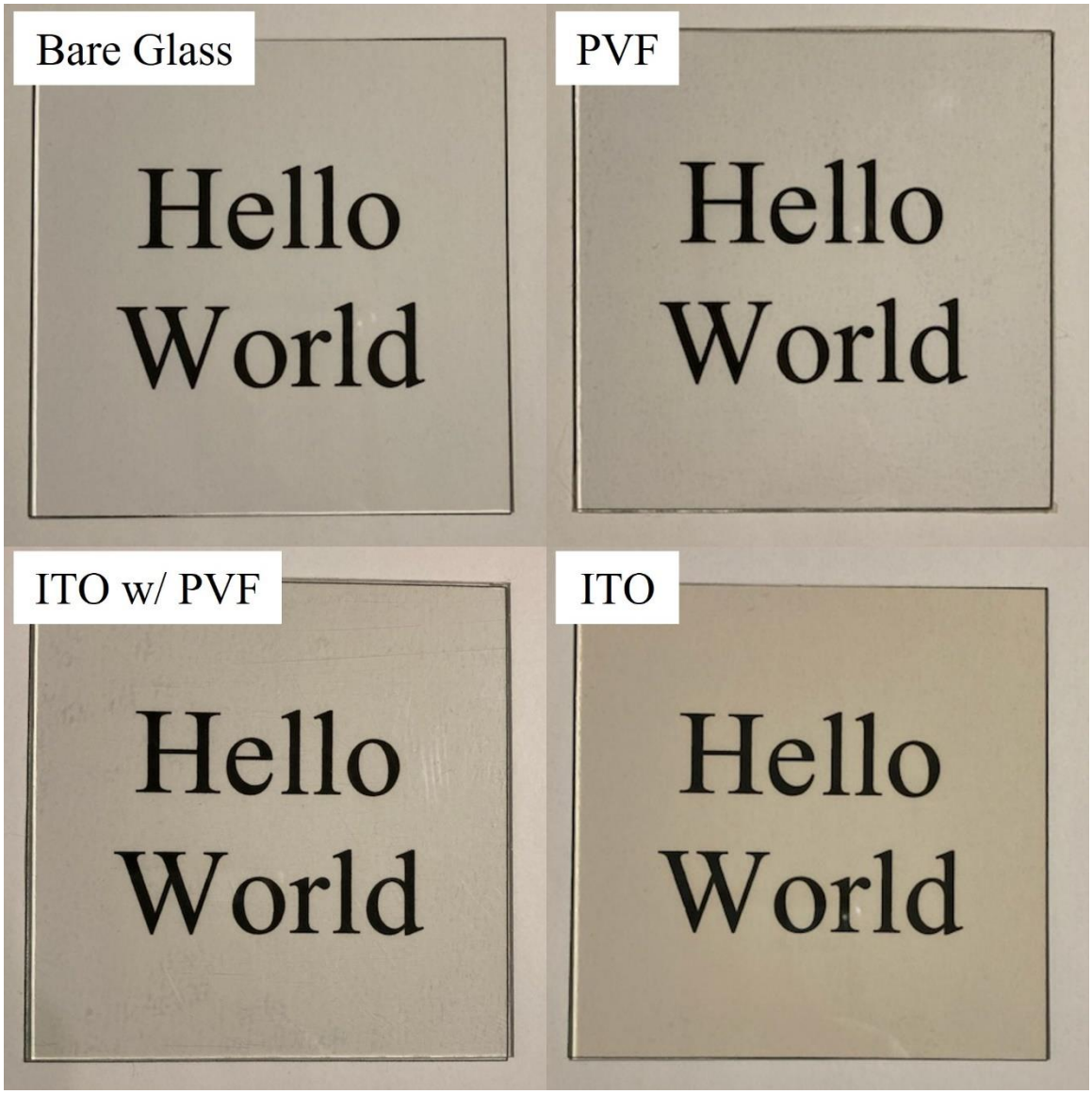

Figure 3.2: Close-up view of experimental glazings on white background with “Hello World” reference text.

3.2 Optical Properties:

Theoretical modelling of the experimental setup required characterizing the optical properties of the glazing surfaces and paper that lines the inner building envelope. The reflectivity and transmissivity of the materials were measured using UV-Vis and

FTIR spectroscopy for wavelengths between 0.3μm and 16.7 μm. The emissivity could then be calculated using equation (18).

$$\varepsilon_\lambda = 1 - \tau_\lambda - \rho_\lambda \quad (\mathbf{18})$$

In equation (18), ε_λ, τ_λ, and ρ_λ represent the spectral emissivity, transmissivity, and reflectivity, respectively. Fig. 3.3 plots the spectral transmissivity of the sky-facing surface of the various experimental glazings. All glazing types demonstrated relatively high transmission in the visible spectrum. Glazings that had an ITO coating tended to have less transmission in the visible spectrum compared to their counterparts. As expected, this trend was even more prevalent in the NIR regime. The transmissivity of all glazing types dropped to zero in the MIR regime because glass is opaque for those wavelengths [20].

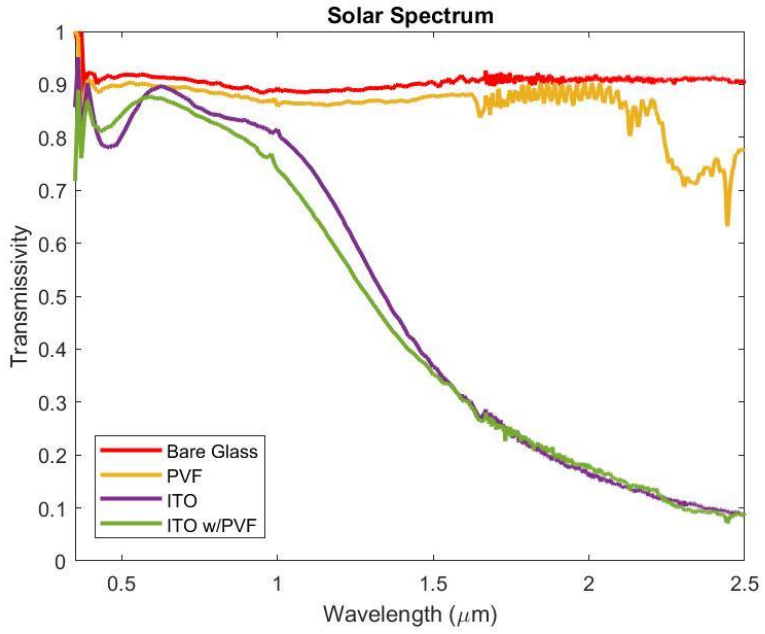

Figure 3.3: Measured spectral transmissivity of sky-facing glazing surfaces in Solar Spectrum

Fig 3.4 plots the spectral reflectivity of the sky-facing surface of the experimental samples. The glass coated only in ITO demonstrated higher reflectivity than its counterparts in the MIR regime. In the NIR regime (up until ~1.5 μm), glass coated only in ITO and glass coated in ITO and PVF demonstrated similar levels of superior reflectivity over their counterparts. Bare glass demonstrated an increase in reflectivity in the atmospheric window as compared to the glazings with a layer of PVF film.

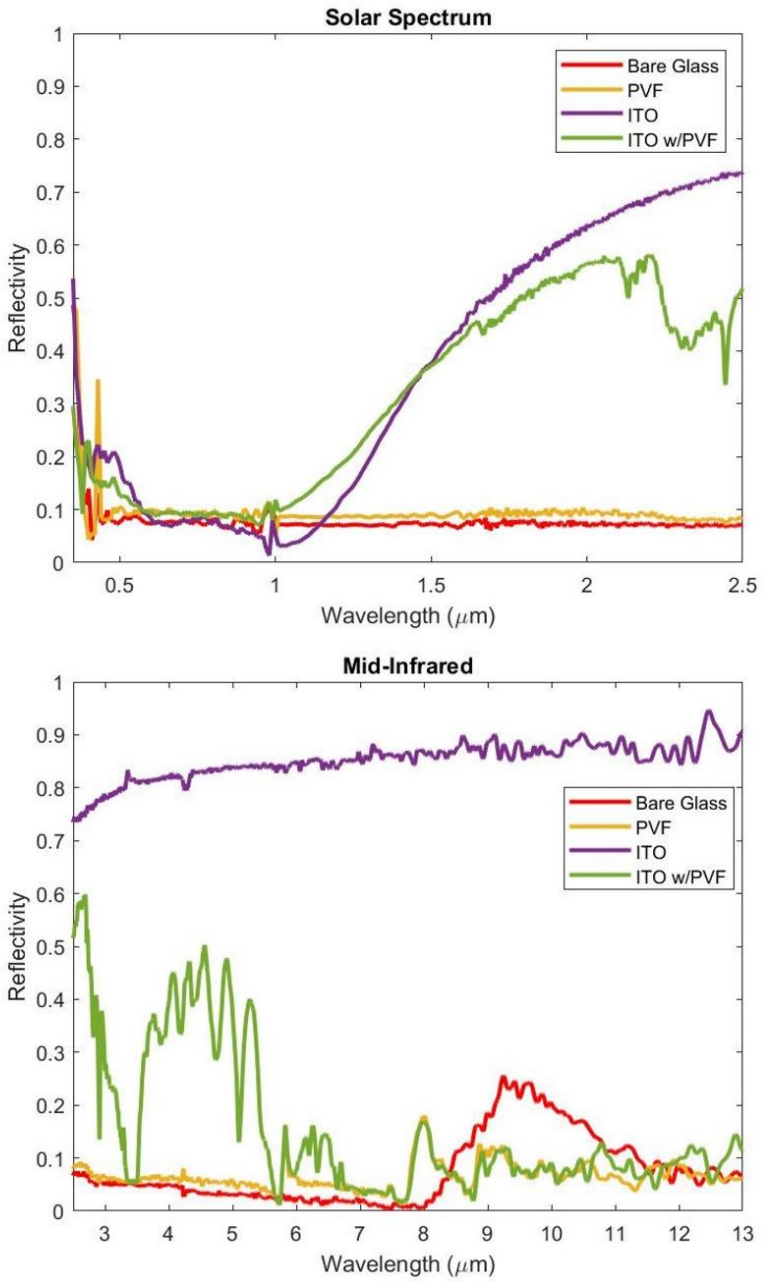

Figure 3.4: Measured spectral reflectivity of sky-facing glazing surfaces in solar spectrum (top) and MIR (bottom).

Fig 3.5 plots the spectral emissivity of the sky-facing surfaces of the experimental samples. Bare glass and samples coated in PVF demonstrated high emissivity in the MIR

regime. PVF coated samples had an emissivity of ~0.9 in the atmospheric window. The sample coated in PVF and ITO showed a drop in emissivity for $\lambda > 13\mu m$; this is beneficial for preventing heat gain from long-wave infrared radiation (LWIR). Glass coated only in ITO demonstrated the lowest emissivity in the MIR regime. This inhibits the absorption of LWIR as well as radiative cooling. In the solar spectrum, glazings that had a coating of ITO demonstrate greater solar absorptivity than their counterparts. Furthermore, the sample coated in ITO and PVF demonstrated a relatively significant solar absorptivity in the latter end of the NIR regime.

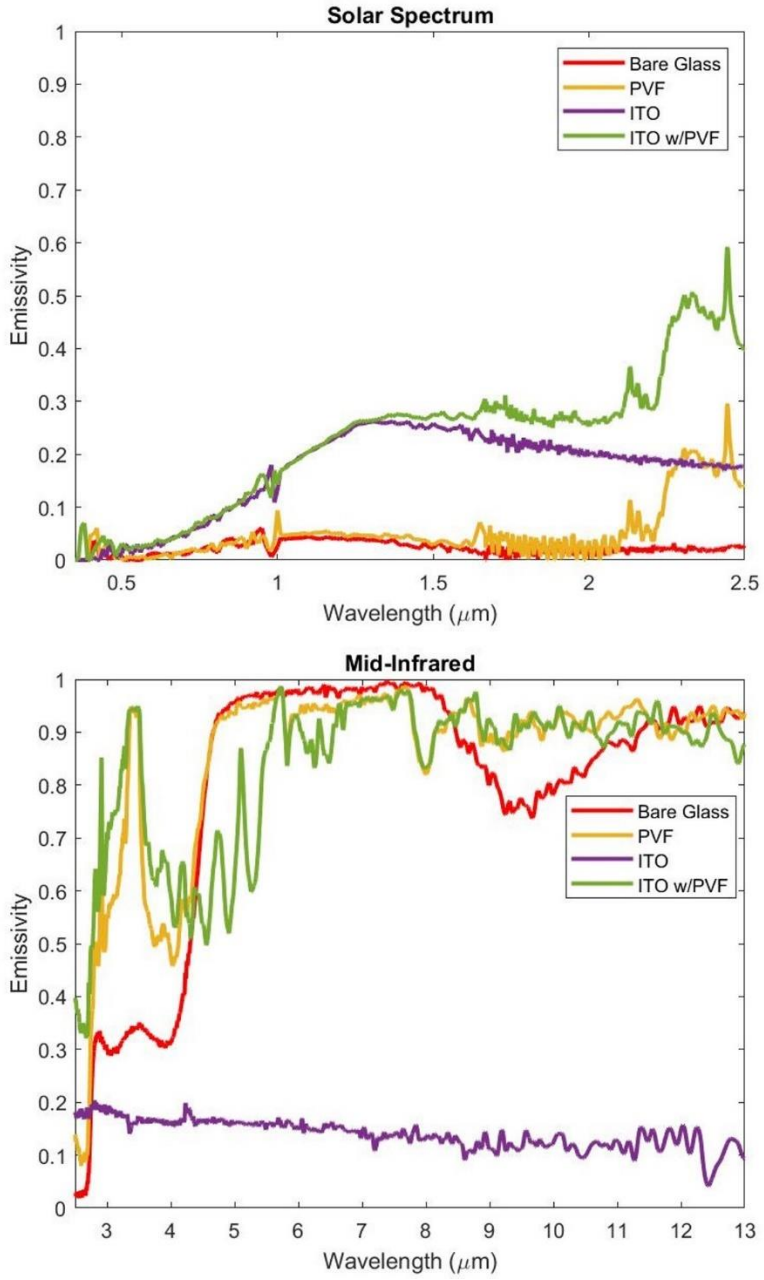

Figure 3.5: Calculated spectral emissivity of sky-facing glazing surfaces in solar spectrum (top) and MIR (bottom).

Since the inward facing surfaces of the experimental samples do not have any form of additional coating or film, it is convenient to only show the emissivity of these

surfaces. The spectral emissivity values for the inward facing surfaces of the experimental samples are presented in Fig. 3.6. For wavelengths greater than ~5 μm, the inward facing surfaces of all the experimental samples behaved like bare glass. Samples coated only in ITO and samples coated in ITO and PVF had near identical emissivity throughout the entire spectrum. In general, the greatest variation in spectral properties between inward facing and sky-facing surfaces occurred with samples coated in ITO. The inner surfaces of ITO coated samples demonstrated emissivity higher than glass for wavelengths less than 4 μm. Unlike the ITO coated samples, the inner facing surface of the sample coated only in PVF, demonstrated behavior that was nearly identical to its sky facing surface.

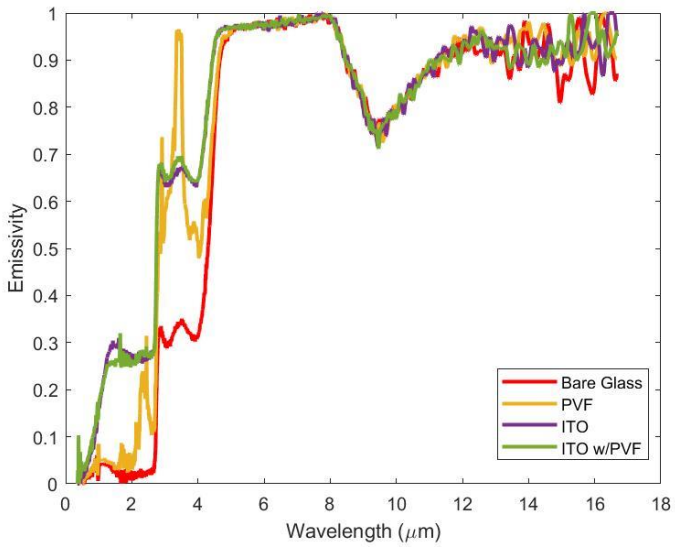

Figure 3.6: Calculated spectral emissivity of inward facing glazing surfaces

Spectral emissivity values of the “black” paper than lined the inner surfaces of the experimental model are necessary to calculate radiative heat exchange within the model enclosure.

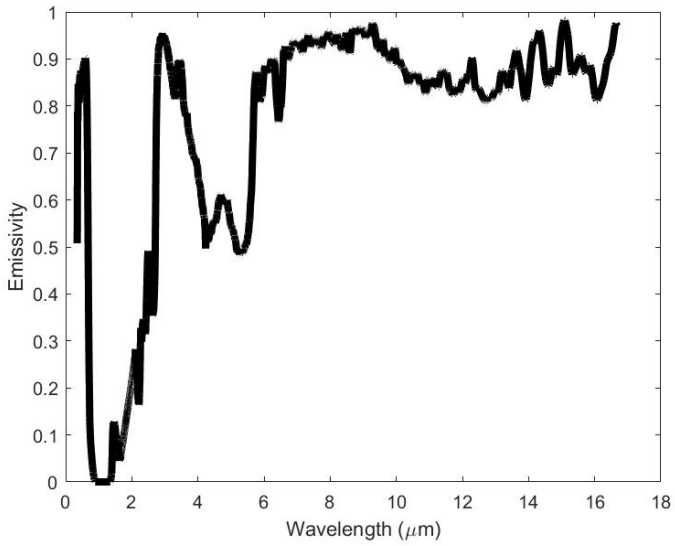

Figure 3.7: Calculated spectral emissivity of paper surfaces

As Fig. 3.7 demonstrates, the "black" paper has a relatively high emissivity value (0.8-0.9) in the visible spectrum. In the NIR regime, the paper lining has a low emissivity value and is highly reflective. The paper lining demonstrates relatively high emissivity in the MIR regime. In general, the paper lining does not approach ideal black body behavior used in the theoretical calculations in Chapter 2.

3.3 Temperature Measurements:

Outdoor field tests were conducted with the experimental setup to demonstrate the cooling performance of the proposed glazing during day and nighttime conditions During each field test, the experimental setup was placed on an unshaded tabletop in Florence, AZ for a period of 24 hours. Temperature measurements of the ambient air as well as the air within the model enclosures were recorded simultaneously at a sampling rate of 0.1 Hz. Three separate field tests were performed to verify the experimental behavior. These field tests took place on October 12, 2022, November 5, 2022, and November 6, 2022

starting at 1:30 am, 12:00am, and 12:00 am, respectively. The resulting recorded temperatures are displayed in Fig. 3.8-3.10.

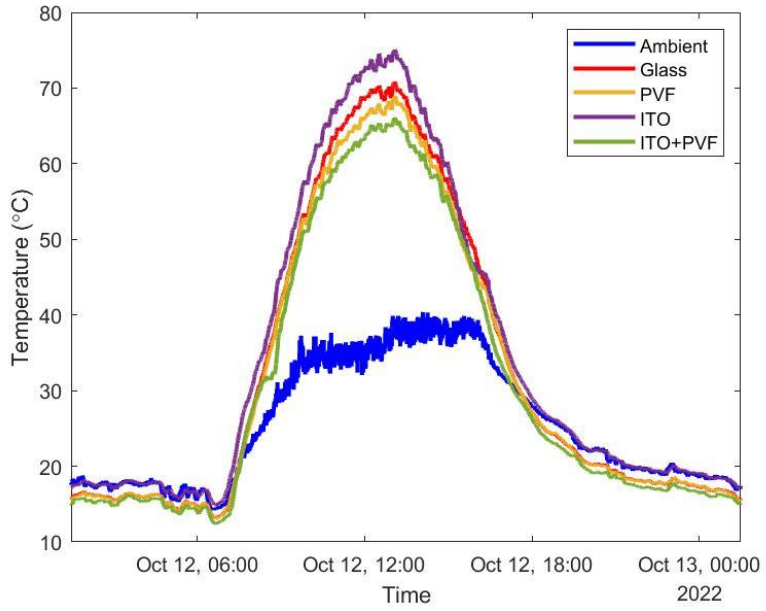

Figure 3.8: Measured temperature values during 24-hour field test on October 12, 2022

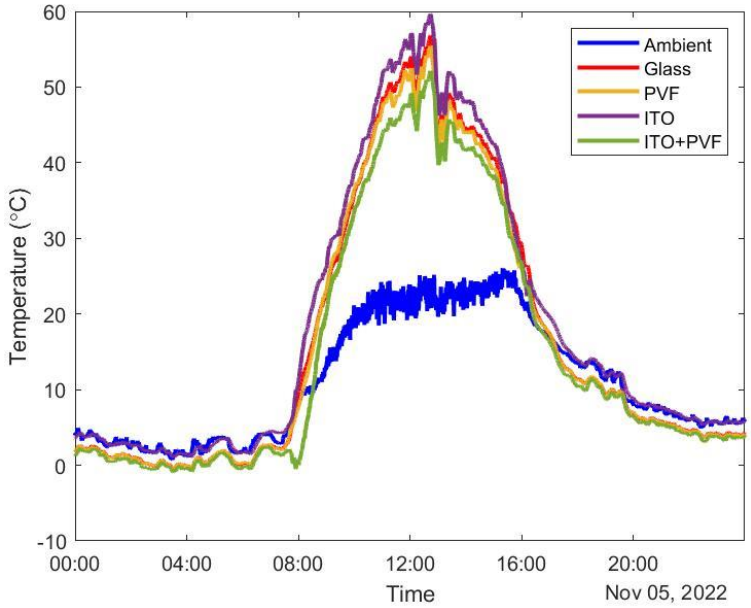

Figure 3.9: Measured temperature values during 24-hour field test on November 5, 2022

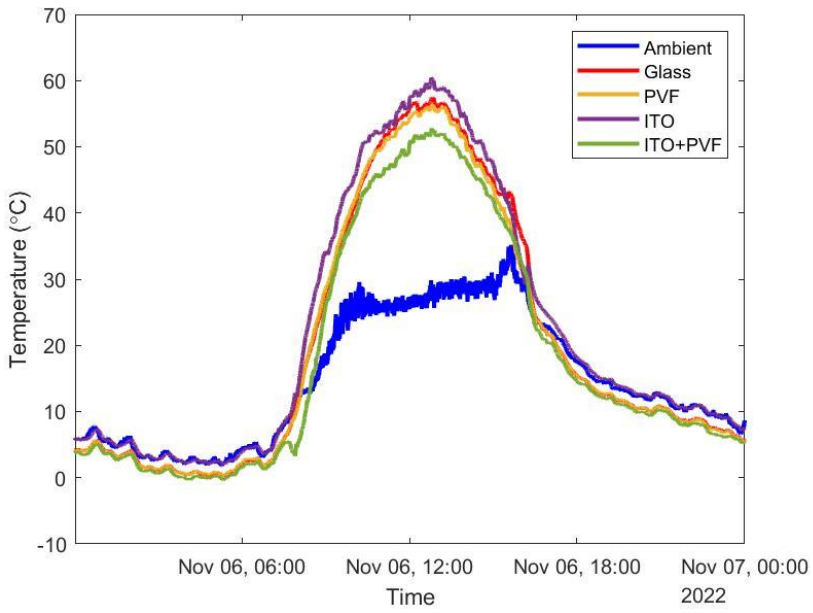

Figure 3.10: Measured temperature values during 24-hour field test on November 6, 2022.

In order to highlight nighttime performance, temperature values recorded between 1:30AM and 5:30AM are isolated in Fig. 3.11-Fig. 3.13. During the nighttime, all experimental samples except for glass coated in ITO achieved consistent sub-ambient cooling. The proposed glazing constructed with ITO and PVF had the greatest nighttime cooling effect. The internal air temperature within the experimental model was about 2℃ cooler than the outdoor ambient temperature. Furthermore, the ITO and PVF coated glazing model demonstrated a maximum nighttime air temperature difference of about 1℃ when compared to conventional glass.

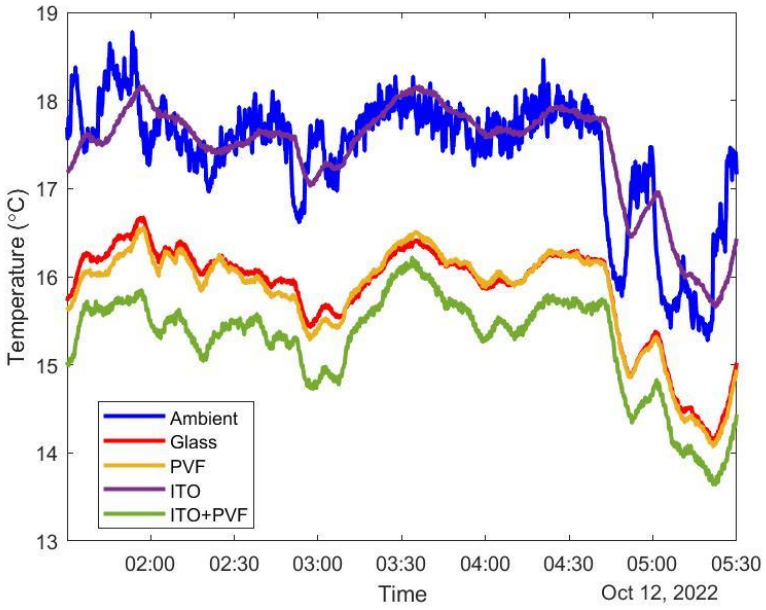

Figure 3.11: Measured nighttime temperatures during field test between 1:30AM and 5:30AM on October 12, 2022.

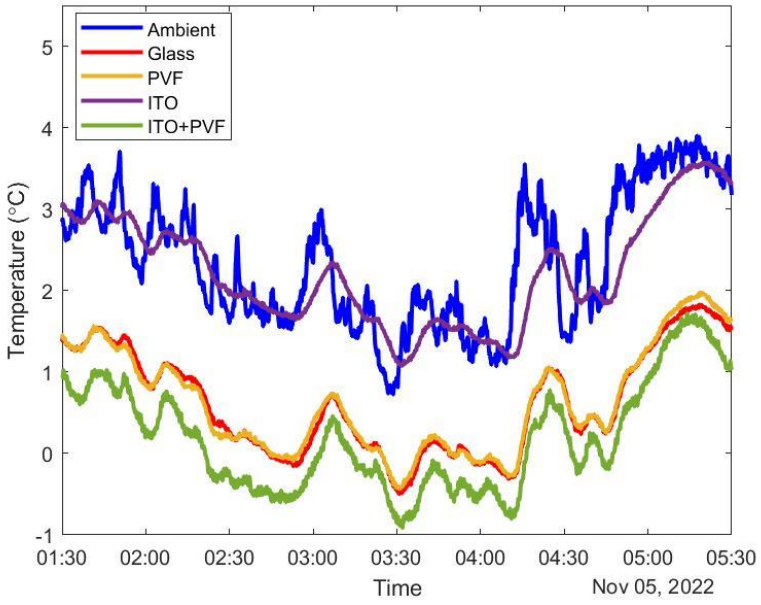

Figure 3.12: Measured nighttime temperatures during field test between 1:30AM and 5:30AM on November 5, 2022.

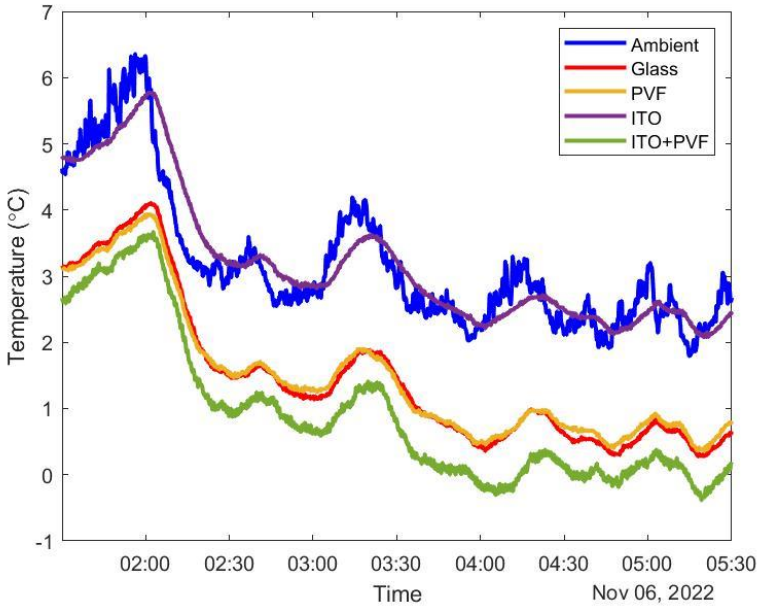

Figure 3.13: Measured nighttime temperatures during field test between 1:30AM and 5:30AM on November 6, 2022.

Similar to Fig. 3.11-3.13, the daytime cooling performance is highlighted in Fig. 3.14-3.16 by presenting the recorded temperature values between 9:30AM and 3:30AM. The internal air within the experimental models never demonstrated sub-ambient temperatures during daytime hours. The glazing constructed with ITO and PVF coating demonstrated the greatest cooling effect among the experimental samples. Compared to conventional glass, the internal air inside the ITO and PVF glazing model demonstrated a maximum temperature difference of ~6 ℃. In general, the glazing coated only in PVF also demonstrated daytime air temperatures cooler than conventional glass. For all three days, the glazing coated only in ITO demonstrated the highest internal air temperatures. It is worth noting that the superior cooling effect demonstrated by the ITO and PVF coating

is attenuated by presence of clouds. This phenomenon is prevalent in Fig 3.15 where the performance of glazing is quite similar to its counterparts during the sharp temperature change just prior to 13:00.

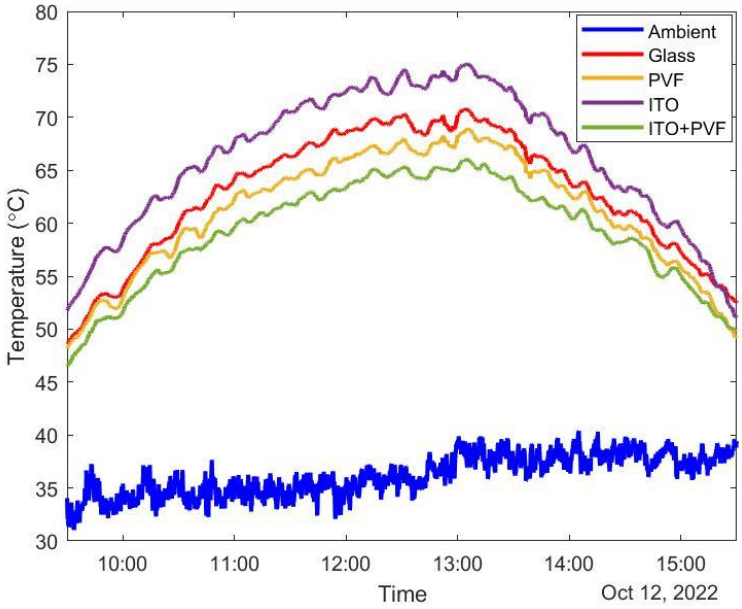

Figure 3.14: Measured daytime temperatures during field test between 9:30AM and 3:30PM on October 12, 2022.

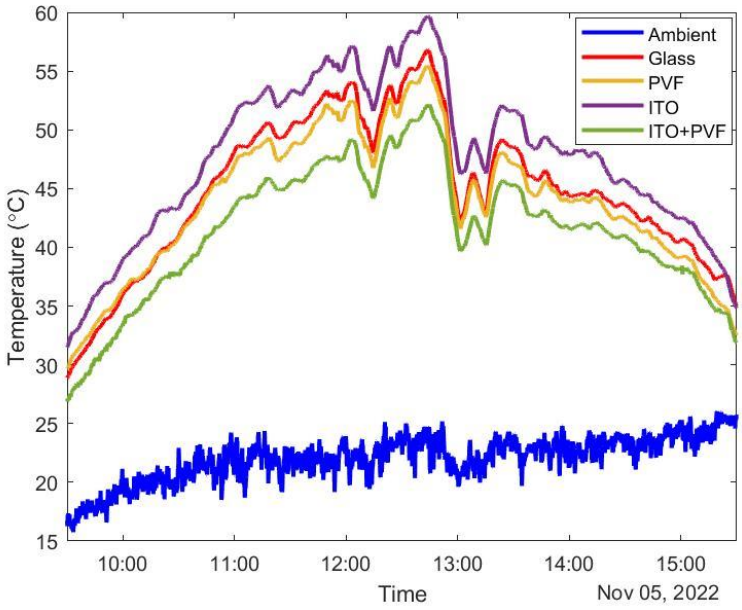

Figure 3.15: Measured daytime temperatures during field test between 9:30AM and 3:30PM on November 5, 2022.

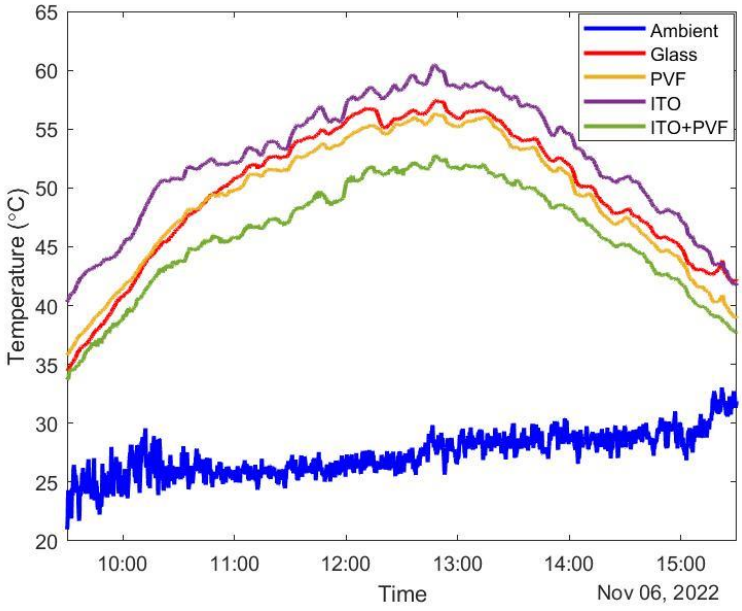

Figure 3.16: Measured daytime temperatures during field test between 9:30AM and 3:30PM on November 6, 2022.

The theoretical model proposed in chapter 2 was used to validate the experimental data. Solar flux and wind speed measurements were recorded manually in 10-minute intervals and used as weather inputs for the heat transfer model. For convenience, the manual measurements were only recorded for a period of 1 hour during the day and night. The time periods being used to validate the experimental data occurred on October 12, 2022, from 2:00pm to 3:00PM during the day and 3:00am to 4:00am during the night. The resulting manual measurements are displayed in Fig. 3.17 and Fig 3.18

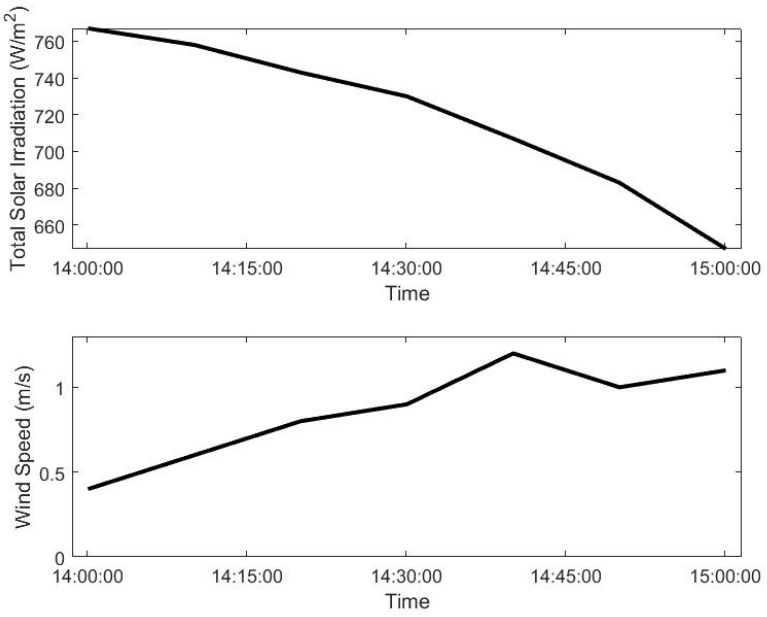

Figure 3.17: Manually recorded daytime solar flux and wind speed measurements taken between 2:00 PM and 3:00 PM on October 12, 2022

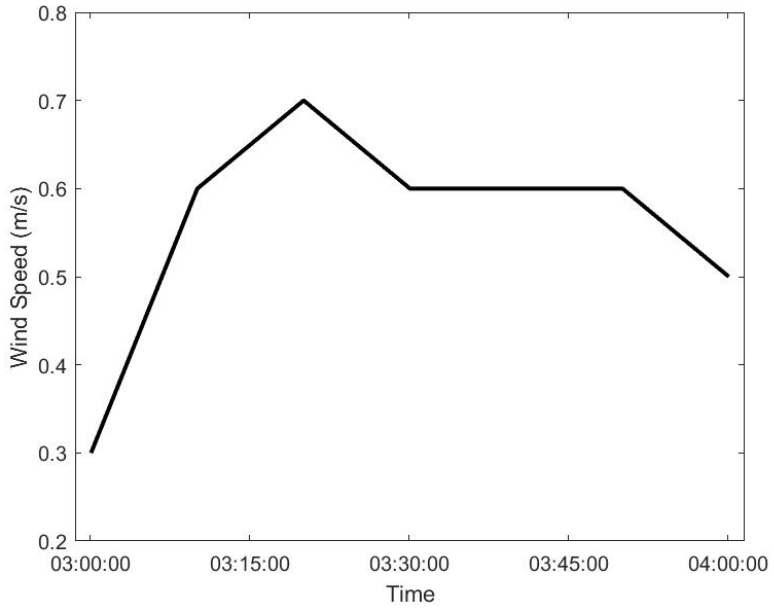

Figure 3.18: Manually recorded nighttime wind speed measurements taken between 3:00 AM and 4:00 AM on October 12, 2022

The nighttime experimental data that was simulated theoretically is shown in Fig. 3.19. From Fig. 3.19, it was expected that the theoretical data would demonstrate a relatively insignificant difference in performance between the bare glass, glass with PVF, and glass with ITO and PVF. Furthermore, it was expected that these samples would demonstrate temperature values that were cooler than those demonstrated by the sample coated in ITO only.

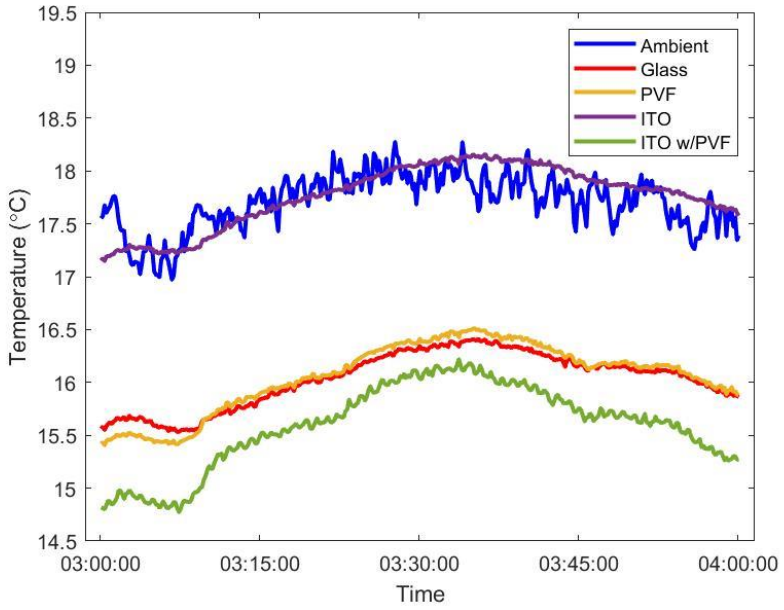

Figure 3.19: Measured nighttime temperature data taken on October 12, 2022 used to validate theoretical model.

For each glazing type, a comparison between the experimental and simulation values are presented in Fig. 3.20 for nighttime conditions. For all glazing types, the nighttime trends of the theoretical model with respect to time are in good agreement with the experimental measurements. On average, the temperature difference between the experimental and theoretical temperature values was 1.49°C and the percent error was 0.52%. For all glazing types, the theoretical model consistently overestimated the temperature drop exhibited by the indoor air. In general, the experimentally measured temperature values were outside the uncertainty limits of the theoretical temperature values. The difference between the experimental and theoretical temperature values could be attributed to unaccounted heat gains via conduction through the walls of the experimental setup.

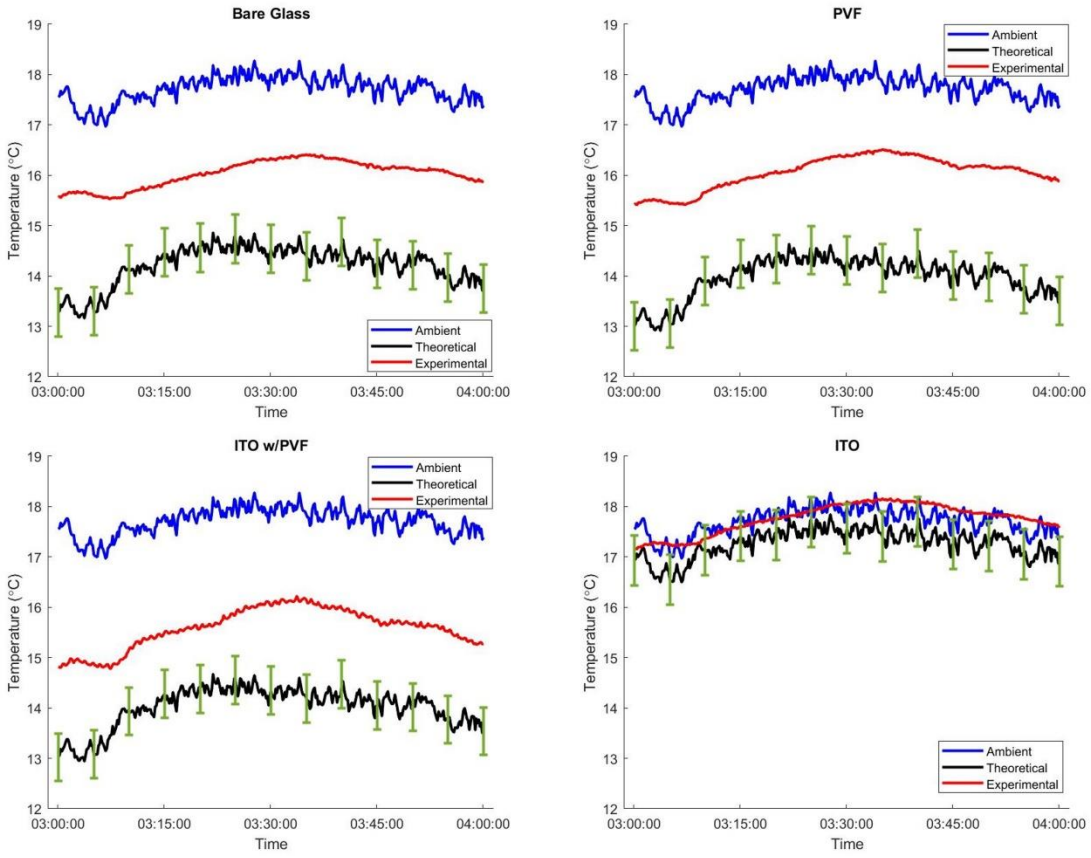

Figure 3.20: Comparison between experimental and theoretical nighttime temperature data for experimental glazings.

Fig. 3.21 is the theoretical analogy to Fig. 3.19. The resulting behavior of the glazings relative to each other is expected. Theoretically, the glazing coated in ITO only, demonstrated the smallest temperature drop amongst the glazing samples. Furthermore, the bare glass, glass with PVF only, and glass with PVF and ITO, showed minimal difference in overall theoretical performance.

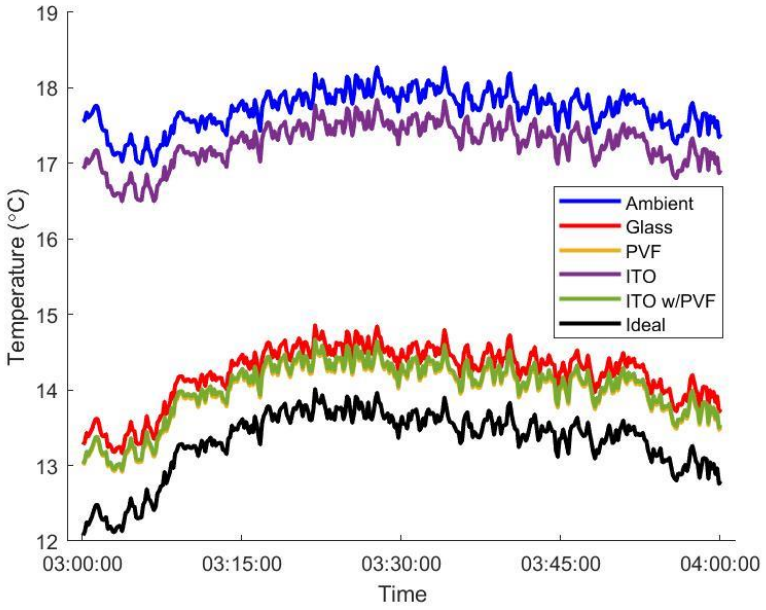

Figure 3.21: Theoretical nighttime temperature values for all glazing types.

For daytime conditions, the theoretical model simulated the experimentally measured results shown in Fig. 3.22. Based on Fig 3.22 and Fig. 3.17, it was expected that the theoretical model would predict decreasing temperature values with respect to time for all glazing types due to the decrease in solar irradiation with time. Additionally, it was expected that the theoretical model would predict superior performance from the PVF coated glazings.

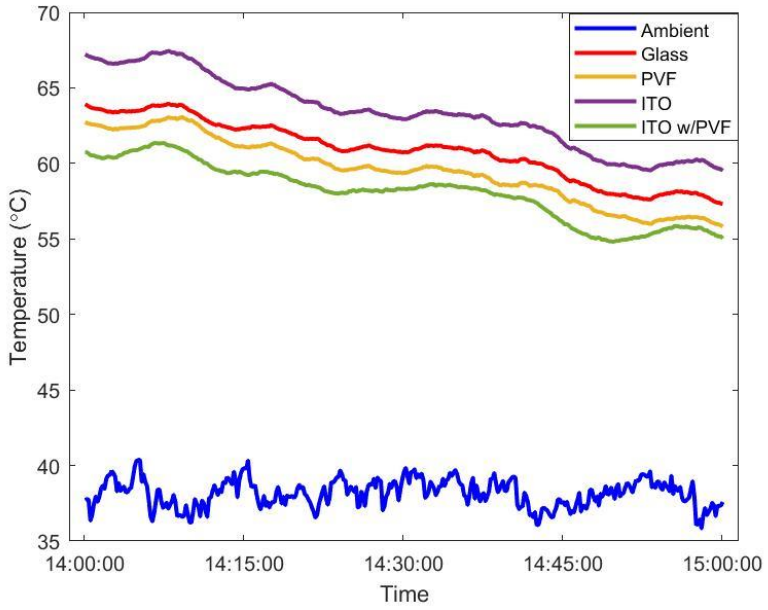

Figure 3.22: Measured daytime temperature data taken on October 12, 2022 used to validate theoretical model.

Similar to Fig. 3.20, Fig 3.23 presents a comparison between the experimental and simulation values for each glazing type during daytime conditions. All glazings demonstrated relative agreement between experimental and theoretical temperature data with respect to time. On average, the temperature difference between the experimental and theoretical temperature values was 1.47℃ and the percent error was 0.44%. The simulation of bare glass and glass with PVF only, slightly overestimated cooling effect when compared to the experimental data. In contrast, simulation of samples with ITO tended to underestimate the cooling effect when compared to the experimental data. Furthermore, the experimentally measured temperature tended to be outside the uncertainty limits of the theoretical temperature for glazings with ITO.

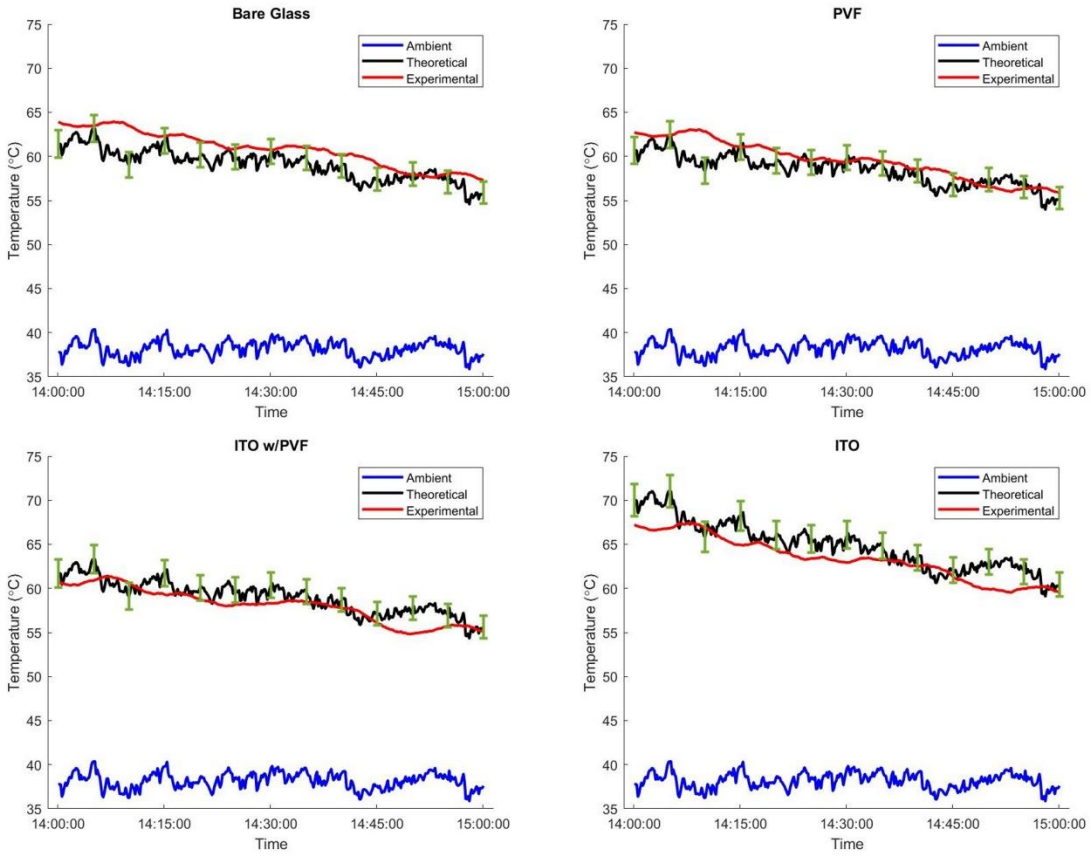

Figure 3.23: Comparison between experimental and theoretical daytime temperature data for experimental glazings.

As seen in Fig. 3.24, the theoretical simulation tends to attenuate the difference in indoor air temperatures for the bare glass, glass with PVF, and glass with PVF and ITO samples. Furthermore, the theoretical model demonstrates no significant difference in temperature values between the aforementioned sample types.

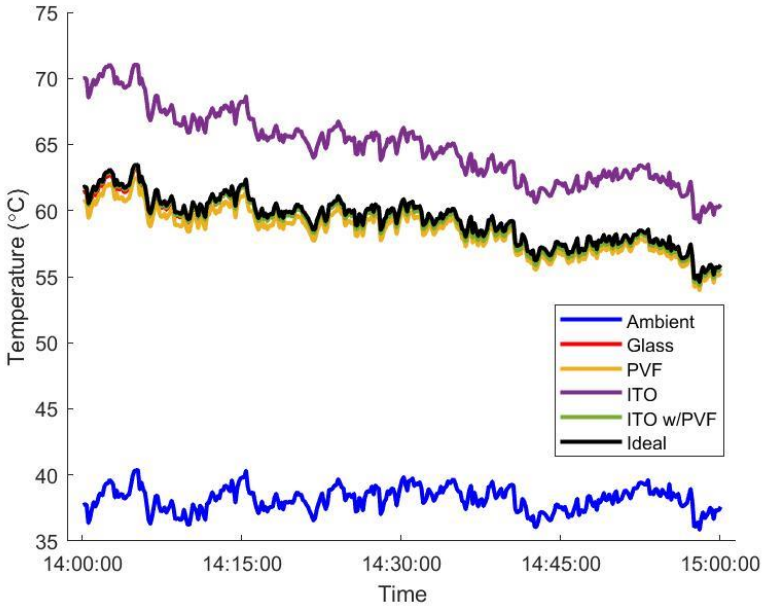

Figure 3.24: Theoretical daytime temperature values for all glazing types.

3.4 Uncertainty Analysis:

In addition to theoretically calculating the internal air temperature for the various glazing types, the uncertainty in each temperature value was calculated. The total uncertainty, U_{T_∞}, for any experimental value is a function of bias uncertainty, B_{T_∞}, and precision uncertainty, P_{T_∞}.

$$U_{T_\infty} = \sqrt{P_{T_\infty}^2 + B_{T_\infty}^2} \tag{19}$$

For the theoretical internal air temperature values, propagation of uncertainty is necessary because its uncertainty is a result of uncertainty in the measured weather condition values (wind speed, solar flux, ambient air temperature). The bias uncertainty is propagated using equation (20). Propagation of precision uncertainty is calculated using

equation (20) except the precision uncertainty of measured values is used instead of the bias uncertainty.

$$B_{T_\infty} = \sqrt{\left(\frac{\partial T_\infty}{\partial T_a} * B_{T_a}\right)^2 + \left(\frac{\partial T_\infty}{\partial V} * B_V\right)^2 + \left(\frac{\partial T_\infty}{\partial G} * B_G\right)^2} \quad (\mathbf{20})$$

In equation (20), B_{T_a}, B_V, and B_G are the bias uncertainty in the ambient air temperature, wind speed, and solar flux measurements, respectively. Since the internal air temperature is calculated by solving an implicit system of equations, it is difficult to evaluate the derivatives in equation (20). As such, a first order approximation is used to evaluate the derivative terms.

$$\frac{\partial T_\infty}{\partial T_a} = \frac{T_\infty|_{T_a+B_{T_a},V,G} - T_\infty|_{T_a,V,G}}{B_{T_a}} \quad (\mathbf{21})$$

$$\frac{\partial T_\infty}{\partial V} = \frac{T_\infty|_{T_a,V+B_V,G} - T_\infty|_{T_a,V,G}}{B_V} \quad (\mathbf{22})$$

$$\frac{\partial T_\infty}{\partial G} = \frac{T_\infty|_{T_a,V,G+B_G} - T_\infty|_{T_a,V,G}}{B_G} \quad (\mathbf{23})$$

Substituting equations (21)-(23) into equation (20) and simplifying yields the final equation used to calculate the bias uncertainty.

$$X = T_\infty|_{T_a+B_{T_a},V,G} - T_\infty|_{T_a,V,G} \quad (\mathbf{24})$$

$$Y = T_\infty|_{T_a,V+B_V,G} - T_\infty|_{T_a,V,G} \quad (\mathbf{25})$$

$$Z = T_\infty|_{T_a,V,G+B_G} - T_\infty|_{T_a,V,G} \quad (\mathbf{26})$$

$$B_{T_\infty} = \sqrt{X^2 + Y^2 + Z^2} \quad (\mathbf{27})$$

Equations (24)-(26) were separated from equation (27) to help maintain clarity.

The bias uncertainty in the in the ambient air temperature, wind speed, and solar flux measurements are necessary to utilize equations (24)-(27). The bias uncertainty in the ambient air temperature readings is due to the accuracy of the K-Type thermocouple. The accuracy of the K-Type thermocouples was checked using icy water (0℃) and was shown to be ±0.5℃; this is also the accuracy for the thermocouples used to measure the internal air temperature within the experimental setup. The accuracy of the anemometer is provided by the manufacturer as ±5% of the measured reading. The accuracy of the solar power meter is provided by the manufacturer as $\pm 10 Wm^{-2}$ or ±5% of the measured reading (whichever is greater). Additionally, the solar power meter has a temperature induced error of $\pm 0.38 Wm^{-2}/℃$ for every degree greater than 25℃.

The precision uncertainty in the internal air temperature values could not be properly evaluated because weather conditions (independent variables) are inherently random. For a given time of day, repeated independent experiments will experience different weather conditions. Therefore, the precision uncertainty of the ambient air temperature, wind speed, and solar flux measurements cannot be quantified. As such, the precision uncertainty was taken to be zero in this analysis ($P_{T_\infty} = 0$).

The result of this uncertainty analysis is displayed as green error bars in Fig. 3.20 and Fig. 3.23. Error bars are presented at data points every five minutes for the sake of clarity. However, the provided method for propagating uncertainty could be applied for all calculated theoretical temperature values.

CHAPTER 4

CONCLUSION AND FUTURE RECOMMENDATIONS

4.1 Conclusion

A window glazing constructed from a soda-lime glass substrate coated in ITO and PVF film was proposed to serve as a visibly transparent, radiative cooling material. The cooling performance of the window glazing was assessed using a framework intended to mimic a building possessing a skylight. This framework served as the basis for an experimental setup that was validated through theoretical modeling.

Outdoor tests with the experimental setup demonstrated that the proposed glazing provided improved day and nighttime cooling performance as compared to glazings constructed from bare glass, glass coated only in ITO, and glass coated only in PVF. Improved cooling performance was demonstrated by reduced air temperatures within the model envelope.

A heat transfer model was developed to simulate the temperature distribution within the experimental setup. This heat transfer model was implemented as a MATLAB code that solved the simultaneous energy balance equations. Since the heat transfer model depends on the optical properties of the glazing surfaces, measurements of the glazing optical properties were taken using UV-Vis and FTIR spectroscopy. Using experimentally measured weather conditions and material properties, the results of the heat transfer model showed relatively good agreement with the field test results.

4.2: Future Work

The primary weakness of the proposed window glazing is that the optical properties are fixed, irrespective of outdoor temperature; the combination of ITO and PVF on traditional window glazings would be disadvantageous in conditions where cooling is unfavorable. Future work would attempt to develop a visibly transparent material with tunable spectral properties. In the NIR, this material would have high emissivity during cold conditions and low emissivity during warm conditions; this would allow the modulation of solar heat gain. Similarly, this material would modulate the radiative cooling effect by having a low emissivity in the atmospheric window during cold conditions and high emissivity in the atmospheric window during warm conditions. Development of such a material would yield desirable results at the cost of increased complexity (and potentially decreased manufacturability).

REFERENCES

[1] Jelle B.P., Hynd, A., Gustavsen, A., Arasteh, D., Goudey, H., & Hart, R. (2012). "Fenestration of today and tomorrow: A state-of-the-art review and future research opportunities," *Solar Energy Materials and Solar Cells*, *96*(1), pp.1–28.

[2] Chen, X., & Zhu, H. (2011). 3.01 - Catalysis by Supported Gold Nanoparticles. In *Comprehensive Nanoscience and Technology, Five-Volume set* (pp. 1–11).

[3] http://rredc.nrel.gov/solar/spectra/am1.5/ National Renewable Energy Laboratory, National Renewable Energy Laboratory, (Date accessed: Dec 30, 2021).

[3] Mandal, J., Huang, X. & Raman, A.P.. (2021). "Accurately Quantifying Clear-Sky Radiative Cooling Potentials: A Temperature Correction to the Transmittance-Based Approximation," *Atmosphere*, *12*(1195).

[4] Zhao, D., Aili, A., Zhai, Y., Xu, S., Tan, G., Yin, X., & Yang, R. (2019). "Radiative sky cooling: Fundamental principles, materials, and applications," *Applied Physics Reviews*, *6*(2), 21306

[5] Raman, A.P., Anoma, M. A., Zhu, L., Rephaeli, E., & Fan, S. (2014). "Passive radiative cooling below ambient air temperature under direct sunlight," *Nature*, *515*(7528), 540–544

[6] Bahadori. Mehdi, N (1978). "Passive Cooling Systems in Iranian Architecture." *Scientific American*, *238*(2), 144–155.

[7] Chow, T., Li, C., & Lin, Z. (2010). Innovative solar windows for cooling-demand climate. *Solar Energy Materials and Solar Cells*, *94*(2), 212–220.

[8] Cuce, E. & Riffat, S. B. (2015). A state-of-the-art review on innovative glazing technologies. *Renewable & Sustainable Energy Reviews*, *41*, 695–714.

[9] Baetens. R, Jelle, B. P., & Gustavsen, A. (2010). Properties, requirements and possibilities of smart windows for dynamic daylight and solar energy control in buildings: A state-of-the-art review. *Solar Energy Materials and Solar Cells*, *94*(2), 87–105.

[10] Kou, J., Jurado, Z., Chen, Z., Fan, S., & Minnich, A. J. (2017). Daytime Radiative Cooling Using Near-Black Infrared Emitters. *ACS Photonics*, *4*(3), 626–630.

[11] Meng, S., Long, L., Wu, Z., Denisuk, N., Yang, Y., Wang, L., Cao, F., & Zhu, Y. (2020). Scalable dual-layer film with broadband infrared emission for sub-ambient daytime radiative cooling. *Solar Energy Materials and Solar Cells*, *208*, 110393–.

[12] Zhao, B., Hu, M., Ao, X., Xuan, Q., & Pei, G. (2020). Spectrally selective approaches for passive cooling of solar cells: A review. *Applied Energy*, *262*, 114548–.

[13] Lee, E., & Luo, T. (2019). Black body-like radiative cooling for flexible thin-film solar cells. *Solar Energy Materials and Solar Cells*, *194*, 222–228.

[14] Yi, Z., lv, Y., Xu, D., Xu, J., Qian, H., Zhao, D., & Yang, R. (2021). Energy saving analysis of a transparent radiative cooling film for buildings with roof glazing. *Energy and Built Environment*, *2*(2), 214–222.

[15] Zhang, X., Li, X., Wang, F., Yuan, W., Cheng, Z., Liang, H., & Yan, Y. (2022). Low-Cost and Large-Scale Producible Biomimetic Radiative Cooling Glass with Multiband Radiative Regulation Performance. *Advanced Optical Materials*.

[16] Modest, Mazumder, S., & Mazumder, S. (2021). *Radiative heat transfer* (4th ed.). Academic Press.

[7] A. Rincón-Casado, F.J. Sánchez de la Flor, E. Chacón Vera, & J. Sánchez Ramos. (2017). "New natural convection heat transfer correlations in enclosures for building performance simulation," *Engineering Applications of Computational Fluid Mechanics*, *11*(1), 340–356.

[18] Çengel Yunus A., & Ghajar, A. J. (2020). *Heat and Mass Transfer Fundamentals and Applications* (6th ed.). McGraw-Hill Education.

[19] Shrestha, Thapa, A., & Gautam, H. (2019). "Solar Radiation, Air Temperature, Relative Humidity, and Dew Point Study Damak, Jhapa, Nepal". *International Journal of Photoenergy*, *2019*, 1–7.

[20] ASHRAE, ASHRAE Handbook: Fundamentals, SI ed., Chapter 35, American Society of Heating, Refrigerating and Air-conditioning Engineers Inc., Atlanta, USA, 2021.